Comparing Anodic Bubble Behavior of Anodes from Anisotropic and Isotropic Cokes in Laboratory Scale Aluminum Electrolysis Cells

Camilla Sommerseth[1,2,*], Rebecca J. Thorne[1,3], Arne Petter Ratvik[2], Stein Rørvik[2], Hogne Linga[4], Lorentz Petter Lossius[4], Ann Mari Svensson[1]

[1]Norwegian University of Science and Technology, Materials Science and Engineering, NO-7491 Trondheim, Norway

[2]SINTEF Industry, NO-7465 Trondheim, Norway

[3]Norwegian Institute for Air Research, NO-2027 Kjeller, Norway

[4]Hydro Aluminium AS, NO-6881 Årdal, Norway

*Corresponding author: Tel: +47 975 79 666. E-mail: camilla.sommerseth@sintef.no

Abstract

During production of aluminum in Hall-Héroult cells, carbon anodes electrochemically oxidize to form mainly CO_2. The CO_2 bubbles block the anode working surface during growth and coalescence, leading to cell voltage loss and voltage oscillations. Lower grade isotropic petroleum cokes are currently being introduced to anodes worldwide, but little is known about effects of coke quality on the unavoidable voltage losses linked to bubble formation. To investigate this, a pilot carbon anode series was made with various blended ratios of isotropic to anisotropic coke. The anodes were characterized with respect to voltage oscillations related to bubble formation and release, wettability towards electrolyte and surface roughness before and after electrolysis. Results showed that voltage noise caused by gas bubbles was reduced for anodes containing isotropic coke. For blended anodes of isotropic and anisotropic coke, the potential oscillation amplitude was reduced by ~0.19 V compared to a 100 % anisotropic coke anode. The percentage of the anode surface screened by gas bubbles was also reduced as isotropic coke was introduced. Increased wettability between electrolyte and two anodes containing isotropic coke was observed after anode polarization. The reduced bubble screening on the anode surface was attributed to better wetting between anode and electrolyte.

1. Introduction

Carbon anodes for the aluminum industry are made from calcined petroleum coke, usually a blend of different anisotropic cokes, anode butts and a coal tar pitch binder. Due to the rapid growth in aluminum production, causing a shortage in traditional anode grade cokes, anode producers have started to explore additions of coke types not previously considered as anode grade coke. As a result, trials of introducing isotropic and more impure cokes into anodes have been initiated by several anode producers (1, 2).

When producing aluminum, aluminum oxide, Al_2O_3, is dissolved in the electrolyte and oxyfluoroaluminate ions are formed. These are oxidized electrochemically on the carbon anode surface to produce CO_2. Although the production of CO gas at the anode is thermodynamically favorable, CO_2 is kinetically favored and the primary gas product at current densities relevant for practical cells (> 0.05 A/cm^2). CO is mainly formed during the cathodic current efficiency loss reaction where CO_2 reacts with dissolved aluminum in the electrolyte (3-5).

Although details of the anodic reaction mechanism are still not fully understood, it is generally agreed that the sequence includes the oxidation of an oxyfluoroaluminate species and an intermediate adsorption process, most likely a CO compound (6). Suggested reaction sequences include (7):

$$AlOF_x^{1-x} + C \rightarrow CO_{ads} + AlF_x^{3-x} + 2e^- \quad (1)$$

$$AlOF_x^{1-x} + CO_{ads} \rightarrow CO_{2\,(g)} + AlF_x^{3-x} + 2e^- \quad (2)$$

Sterten (8) studied NaF-AlF_3 mixtures saturated in alumina in order to determine the oxygen-containing species in the melt. By thermodynamic modelling he suggested that the main species is $Al_2OF_6^{2-}$ and $Al_2O_2F_4^{2-}$, but also that $Al_2O_2F_6^{4-}$ and $Al_2OF_{10}^{6-}$ were possible anions present in the electrolyte.

Kisza, Thonstad and Eidet (9) suggested that the $Al_2O_2F_6^{4-}$ anion was the most likely species in Al_2O_3 rich electrolytes, however, the exact species in the electrolyte could not be proved from their electrochemical measurements. Equations 3 and 4 show their suggested reaction mechanism. The first step is the charge transfer step with an adsorbed intermediate (Equation 3), which was found to be rate determining.

$$Al_2O_2F_6^{4-} + C \rightarrow CO_{ads} + Al_2OF_6^{2-} + 2e^- \quad (3)$$

$$Al_2O_2F_6^{4-} + CO_{ads} \rightarrow CO_2 + Al_2OF_6^{2-} + 2e^- \quad (4)$$

The overpotential related to the anode reaction makes a significant contribution to the overall voltage loss (10). The various contributions that make up the measured anode voltage are provided in Equation 5 (6).

$$E_{anode,measured} = E^{rev} + \eta_c + \eta'_r + \eta_h + I(R'_s + \delta R_s) \quad (5)$$

Here, E^{rev} is the reversible potential for the CO_2 forming reaction, and η_c is the concentration overpotential caused by concentration gradients of Al_2O_3, or more correctly oxyfluoroaluminate ions, in the electrolyte close to the anode. η'_r is the anode reaction overpotential with no bubbles

72 screening/blocking the anode surface and η_h is the additional reaction overpotential due to the
73 reduced effective surface area when bubbles are screening the anode, also known as hyperpolarization
74 (quantified to approximately 15 mV at 1.0 A/cm^2) (11). The total reaction overpotential $\eta_r=\eta'_r+\eta_h$ is
75 related to charge transfer reactions where intermediate adsorption/desorption processes take place
76 on the electrode surface. The last term of Equation 5 is related to the increase in ohmic resistance due
77 to bubbles screening the anode surface: I is the applied current, R'_s gives the ohmic series resistance
78 with no bubbles screening the surface and δR_s denotes the increase in ohmic series resistance due to
79 partial anode blockage.

80

81 Screening of the electrode surface by bubbles introduces a significant contribution to the cell voltage
82 drop and is estimated to result in a voltage increase of around 0.1 to 0.2 V in industrial cells (12).
83 Reducing this parameter thus also means reducing the total energy consumption in Hall-Héroult cells
84 (10). A review of available literature data is provided in the sections below.

85

86 Jones, Evans and Galvin (13) described bubble nucleation theory on surfaces with cavities. These
87 cavities must meet certain criteria with respect to shape, in particular the depth vs. diameter,
88 depending also on the liquid-solid wetting angle. Classical theory of nucleation of gas bubbles forming
89 in a bulk liquid suggests that the solution must be supersaturated with gas (13). In Hall-Héroult cells,
90 the formation of CO_2 will mostly occur at the rim of the pores, where the electrolyte is supersaturated
91 with CO_2. After nucleation of a bubble, buoyancy will lift the new bubble into the closest cavity.
92 Einarsrud (14) suggests that the most relevant bubble nucleation model for carbon anodes in cryolite
93 melts is the Type IV model described by Jones, Evans and Galvin (13). According to this theory, there
94 are no energy barriers related to formation of gas bubbles on nucleation sites. The pores present on
95 the surface will constantly be filled. The process is mass transfer driven and related to the
96 concentration difference of dissolved CO_2 between the bulk and the bubble surface. When the bubble

reaches a critical radius in a given pore, the growth of the bubble at the nucleation site is terminated. The bubble will then detach and start moving along the anode surface. Further growth of the gas bubbles occurs by coalescence, and this process is likely the main mechanism for bubble growth (15, 16). In laboratory scale experiments with transparent cells (17, 18) the time interval between bubble release from the anode surface to generation of new bubbles was found to be very short. This indicates that little supersaturation is needed in order to initiate bubble nucleation, which is evidence that the process is mass transfer driven. Pores are filled with gas from the anode reaction and this is where new bubbles nucleate. Pores on the anode surface are hence important as nucleation sites for gas bubbles.

Several works report a quasi-periodical dynamic pattern of voltage oscillations, related to the additional voltage induced by the gas bubbles e.g. (14, 17-25). The lowest potential during the voltage oscillations are normally attributed to an anode surface free of bubbles. Kiss and Ponscák (15) found through mathematical modelling that the voltage oscillations are mainly governed by coalescence, and that the nucleation stage is completely overshadowed by coalescence. Einarsrud (14) modelled the effect of pore size at constant pore density and found that smaller pores are correlated to elevated bubble release frequencies and voltage oscillation amplitudes. This is explained by the greater amount of potential nucleation sites present, and thereby nucleation frequencies, ultimately leading to larger anode surface coverage at a faster rate compared to cases with larger pores.

The size of the anodes will also affect the voltage oscillations. Larger anodes give higher amplitudes and lower characteristic frequency. This is attributed to the increased length the bubbles will have to travel, giving the bubbles more time to coalesce and block the anode. Einarsrud and Sandnes (26) observed bubbles evolving from an industrial sized anode in a real Hall-Héroult cell, and their findings suggest that several large bubbles are escaping the anodes, producing a more noisy voltage response. This is opposed to their laboratory experiments with smaller anodes (100 mm x 100 mm) where a more

regular voltage oscillation response can be attributed to nucleation and growth of many small bubbles, which coalesce into one single bubble that blocks a large part of the anode. When the bubble blocks the anode surface the voltage rises to a maximum level before the bubble is released, hence causing the voltage to drop. These findings are also visually supported in a study using a see-through cell, with and without slotted anodes (27).

Einarsrud et al. (21) developed a multiscale mathematical model describing voltage oscillations and compared the modelled results to results obtained in a laboratory scale cell. A good agreement between modelled results and experimental results for various bath compositions could only be obtained by accounting for the surface tension and wetting properties of the bath. Current density has also been shown to affect bubble build-up and release. Increasing current density has been shown to increase the bubble frequency and the voltage amplitude (17, 20, 25), which has also been confirmed by CFD models (21). Increasing current density has also been found to give increasing bubble screening and the same was found for decreasing Al_2O_3 content (12). On the other hand, a slight reduction of the bubble screening was observed at increased current densities in a see-through cell (18). The reason for this was not explained, but it should be noted that the geometry of the anode and the cell was different from typical laboratory cells. Cassayre et al. (28, 29) observed in a transparent cell that, at low current densities, bubbles nucleate on specific nucleation sites. With increasing current density, the amount of nucleation sites increases, and the average diameter of bubbles before release is reduced. They also found that the average bubble diameter before release was not affected by the Al_2O_3 content.

The average screening of anodes due to bubbles, and thus the magnitude and frequency of the voltage oscillation, is strongly dependent on the exact cell configuration and varies between industrial cells and laboratory scale cells. Examples from the literature include laboratory scale experiments by Aaberg

et al. (19) with graphite anodes, where the maximum bubble layer coverage of the anode surface was determined to be in the range 65-90 % and average bubble coverage was found to be 45 %. Similarly, Zhao et al. (18) reported a maximum bubble coverage in the range of 70-90 % (average of approximately 60 %) for graphite anodes at 1.0 A/cm^2. A maximum coverage of around 50 % has been suggested for industrial cells (30). Thorne et al. (20) showed that the screening of the anode surface was highly dependent on the anode material, with bubble coverage highest on graphite anodes, intermediate on anodes made from anisotropic coke and lowest on anodes made from isotropic cokes. The bubble coverage in this work ranged from 10 % (isotropic and highly porous anode) to 75 % (graphite) at 1.0 A/cm^2.

Studies on the effect of properties of the carbon anode on the gas bubble behavior are limited in the open literature. Many studies have used graphite, e.g. (17, 18, 25, 28, 29), but studies where industrial anode coke material was utilized are rather scarce. Kasherman and Skyllas-Kazacos (31) made two anodes of the same coke and pitch and made one anode more porous than the other by adding additional coke fines. They found that the ohmic voltage drop through the electrolyte was lower for a more porous anode (compared to a denser anode), implying that the screening of bubbles is lower for the more porous anode. In addition, results suggested that both coke anodes had a lower bath resistivity than the graphite anode. Consequently, the authors suggested that the type of carbon affects the anode-electrolyte wetting properties, but this was not confirmed by specific wetting experiments.

Thorne et al. (20) studied anodes made with different single source cokes. Two anodes were made from anisotropic cokes and two anodes were made from isotropic cokes. The authors found that the frequency of bubble release, voltage oscillation magnitude, bubble volume and degree of bubble screening was affected by the anode quality. Anodes made from isotropic cokes showed a lower

bubble release frequency, had lower potential oscillations, a larger bubble volume and a lower fraction of the surface screened by bubbles screening than anodes made from anisotropic cokes. The anodes made from isotropic cokes showed a lower wetting angle as obtained by the sessile drop method, but in addition, one of them had significantly larger pores, and both had high permeabilities compared to the anodes made from anisotropic cokes. Differences in surface roughness might thus also have influenced the wetting results.

In the present work, the overall goal was to better understand the behavior of the unconventional isotropic coke, which is high in sulfur and impurities compared to the conventional, lower-impurity anisotropic coke. Traditionally, anodes made from 100 % isotropic cokes have not been considered realistic in industrial full scale due to the higher thermal expansion which may cause anode cracking. In the present laboratory experiments, pilot scale anodes were made where the content of isotropic coke to anisotropic coke was varied from 0 %, 7.2 %, 14.2 %, 35.0 %, 49.0 % to 100 %. Thus, compared to the previous work (20), this study was focused on two materials only, one isotropic coke type and one anisotropic coke type. The anodes were characterized in terms of pore size distribution (optical and Hg porosimetry), surface roughness (optical, before and after electrolysis), and were also investigated by electrochemical techniques in laboratory scale experiments to study the build-up, coverage and release of gas bubbles. The wetting properties of the anodes were studied under electrochemical polarization by the immersion-emersion technique (32, 33). In situ electrolyte-anode wetting interactions were also characterized by capacitance measurements. In this manner, the voltage oscillations due to bubble formation could be correlated to the various anode properties and in particular the role of the material vs. the role of the porosity.

2. Experimental

Pilot Anodes and Electrolyte

Pilot scale anodes (Ø = 130 mm, h = 180 mm) were produced by Hydro Aluminium from one single source industrial sponge type anisotropic petroleum coke, one single source isotropic petroleum coke and one industrial grade coal tar pitch. The particle size of the aggregate was limited to 0-2 mm, to ensure a representative and homogeneous working anode surface area in laboratory scale experiments. The recipe for producing the anodes was varied throughout the series in terms of the blending ratio of isotropic to anisotropic coke. The coke aggregate had coke particle fractions of 1-2 mm, 0-1 mm and fines of ball mill dust of less than 63 µm size. Six pilot anodes were produced with different blending ratios. Table 1 shows production details of the anodes where the anode name reflects the isotropic coke content. A graphite material supplied by Svensk Specialgrafit AB (Ultrapure grade CMG) was used for comparison and is denoted as "graphite". The mean grain size of this graphite material was 76 µm and the density was 1.771 g/cm^3. The pitch binder used for production of the anodes had a Mettler softening point of 119.1 °C according to ISO 5940-2:2007 (34) and a quinoline insoluble (QI) level of 7.8 % according to ISO 6791:1981 (35).

Physical Analysis

The volumetric density of the anodes was determined on test pieces of Ø=50 mm diameter and 120 mm height according to ISO 12985-1:2000 (36). Permeability was characterized using an in-house method developed at Hydro comparable to ISO 15906:2007 (37). The elemental composition of metal and sulfur impurities in the carbon anodes were determined using X-Ray fluorescence (XRF) according to ISO 12980:2000 (38). A Micrometrics Autopure IV 9500 Mercury Porosimeter was used to investigate the microporosity. Porosity was also investigated using an optical microscope (high-end Leica/Reichert MeF3A metallurgical optical reflected light microscope) and a custom written macro for the NIH software as described by Rørvik and Øye (39). The porosity size range of the measurements using this method was 5-10000 µm diameter. Two parallel samples were tested for all these analyses.

Surface roughness investigations of the same horizontal anode surface before and after electrolysis at 1.0 A/cm^2 were performed using an Infinitefocus confocal microscope from Alicona. Prior to electrolysis, 10 mm core samples of the horizontal working surface of the 0 %, 49.0 % and 100 % isotropic coke anodes were ground using SiC paper stepwise down to P#4000 grit, and the entire horizontal surface was scanned with the microscope at a vertical resolution of 410 nm. A 3D image of the anode surface including pits and voids was created. The surface roughness of the anode is reported as true area over projected area (TA/PA), where true area included all pits and voids and projected area was the geometric surface area. The rod-shaped samples were electrolyzed at 1.0 A/cm^2 for 1500 s. After electrolysis the remaining electrolyte on the anode surface was removed by soaking in a solution saturated in $AlCl_3$. Confocal microscopy was then repeated to investigate the changes in surface roughness (TA/PA) after electrolysis. Two repeats were run.

Wetting Properties of Polarized Anode Samples in a Cryolitic Melt

An in-house made apparatus (32, 33) was used for investigating the wetting properties of carbon anode samples towards cryolitic melts before and after polarization. The set-up was designed to measure the weight of samples during immersion/emersion in an electrolyte. The test piece was a cup shaped anode with an outer diameter of 30 mm and inner diameter of 22 mm. The anode was kept in a fixed position and the crucible with the electrolyte was moved vertically. The sequence of the measurements was:

- **Step 1:** The sample was positioned 8 mm above the electrolyte. The dry anode sample was immersed 40 mm into the cryolitic melt at a rate of 0.2 mm/s by raising the crucible holding the electrolyte. The sample was left at this position for 10 mins. After 10 mins the crucible was lowered 5 mm at a rate of 0.2 mm/s and left at this position (anode immersed 35 mm) for

another 10 mins until the crucible was lowered at a rate of 0.2 mm/s until the entire anode was out of the electrolyte.

- **Step 2:** The same procedure as above was repeated immediately with the wet sample.
- **Step 3:** The sample was positioned 8 mm above the electrolyte. The wet anode sample was immersed 40 mm into the electrolyte at a rate of 0.2 mm/s, and then held for 10 mins. An anodic current of 0.7 A/cm^2 (50 A, maximum current for the current supplier) was applied for 10 s. The crucible was then lowered at a speed of 0.2 mm/s until the anode was out of the electrolyte.
- **Step 4:** The sample was positioned 8 mm above the electrolyte. The wet anode was immersed 40 mm into the electrolyte at a rate of 0.2 mm/s, and then the direction of the crucible motion was immediately reversed at the same rate.

The measured weight, m_m, of the anode sample during an experiment includes: 1) the free weight [g] of the anode sample, m_0 (i.e. hanging freely over the electrolyte), 2) the buoyancy of the immersed part of the anode sample, m_b, and the weight of the meniscus, m_σ, (32). Thus, for m_m and m_σ:

$$m_m = m_0 + m_b + m_\sigma$$

$$m_\sigma = m_m - m_0 - m_b = m_m - m_t \quad (6)$$

Theoretical weight m_t is given as the sum of the buoyancy and the free weight, i.e. $m_t = m_0 + m_b$.

Equation 7 gives the force [N], F, acting on the anode sample in the vertical direction.

$$F = L \cdot \sigma \cdot cos\theta \quad (7)$$

In the Equation, L is the length of the meniscus [m] (=π(diameter$_{outer}$+diameter$_{inner}$)), σ is the surface tension [N/m] between the liquid and the gas and θ is the calculated wetting angle between the electrolyte and the anode sample. σ was found to be 0.1131 N/m by assuming that Equation 8 applies (6).

$$\sigma = c - d \cdot t \quad (8)$$

Here, c=205.2 N/m and d=0.0921 N/m·°C (6), t = 1000 °C as reported by Fernandez and Østvold (40). The weight of the meniscus can be found by dividing the force by the standard gravity as shown in Equation 9.

$$m_\sigma = \frac{F}{g} \quad (9)$$

Electrochemical Characterization

The electrochemical behavior of the anodes related to bubble formation was investigated using a flat horizontal anode surface, positioned face-down in the electrolyte. 10 mm core anodes were placed inside a boron nitride tube (wall thickness of 2 mm) in order to maintain a completely flat surface (0.79 cm^2) with no vertical anode area exposed to the electrolyte. Shielding was not applied to the electrodes that were subject to investigations by the optical microscope before and after electrolysis. The anode sample was immersed approximately 0.5 cm into the electrolyte. A graphite crucible was used to hold

the electrolyte. The electrolyte was a cryolitic melt (Sigma Aldrich, >97 % purity) with a molar ratio (cryolite ratio, CR) of NaF to AlF_3 of 2.3, with 9.4 wt% γ-Al_2O_3 from Merck (>99.4 % purity), which meant saturated in aluminum oxide, and with an excess of AlF_3 of 9.8 wt% (industrial grade, sublimed in-house). The electrolyte was saturated in aluminum oxide to keep the conditions during the experiments as similar throughout the course of each experiment, as possible. A silicon nitride tube was used to shield the walls of the crucible. The bottom of the graphite crucible acted as cathode to obtain as straight current lines as possible. The anode sample with the boron nitride shielding was threaded onto a Ø = 3 mm stainless steel rod for electrical contact. An aluminum reference electrode was used for all experiments, and a new reference electrode was used for every duplicate experimental run. Figure 1a shows a sketch of the experimental setup. The experiments were performed in a tube furnace at 1000 °C in an argon atmosphere. A Parstat 4000 potentiostat/galvanostat/EIS analyzer from Princeton Applied Research with a minimum/maximum current range of ±40 pA/±4 A was used for the electrochemical testing. A current density of 1.0 A/cm^2 was applied for 2x200 s and the characteristic potential oscillations due to bubble build-up and release were recorded. The first 200 seconds was used as a preconditioning of the anode surface. The volume of released bubbles was calculated using the average of five time-intervals, (Δt) for complete bubble oscillations. Equation 10 shows how the number of moles of CO_2 gas was calculated using Faraday's law. I is the applied current equal to 1 A/cm^2 (0.7854 A), Δt is the average time-interval for complete bubble oscillations, n is the number of electrons passed in the reaction and F is Faradays constant (96485 C/mol). Equation 11 shows how the bubble volume, V_{CO2}, in mL was calculated using ideal gas law. n is the number of moles CO_2 calculated from Equation 10, R is the gas constant 0.0821 L·atm·K^{-1}·mol^{-1}, T is the temperature in the electrolyte equal to 1273 K and P is the atmospheric pressure, assumed to be 1 atm.

$$n_{CO_2} = \frac{I \cdot \Delta t}{nF} \quad (10)$$

$$V_{CO_2} = \frac{n \cdot R \cdot T \cdot 10^3}{P} \quad (11)$$

By applying a constant potential of 2.5 V for 200 s, while the current was recorded, the bubble coverage, also denoted as bubble screening, on the anode surface was determined by calculating the ratio between the average maximum and average minimum current values (I_{max} and I_{min}), according to Equation 12. It is assumed that no bubbles are covering the anode at I_{min}. Bubble layer thickness was not included in the calculations due to the small size of the anodes in this work. This is in accordance with similar calculations in Thorne et al. (20). Since the bubble layer thickness has not been taken into consideration in this calculation it can only give an indication on the gas bubble screening.

$$Gas\ bubble\ screening = \frac{I_{max}}{I_{min}} \cdot 100\ \% \qquad 12$$

Three to five samples were tested for each anode material except for the 7.2 % isotropic coke content anode. The test sequence of the anode series was randomized during the experiments to eliminate possible changes in the properties of the melt over the course of the experiment. This includes changes in impurity level in the electrolyte and changes in surface tension between anode and electrolyte. After one round of electrochemical testing, the 7.2 % isotropic coke anode was excluded due to the relatively small amount of isotropic coke on the small working anode surface. The risk that the working surface only contained anisotropic coke was considered too high.

For the electrochemical impedance spectroscopy measurements (EIS), a different configuration for the working electrode was used, with the exposed surface area vertically oriented in the melt, as shown in Figure 1b and c. This configuration is necessary to minimize the bubble noise in the experiment. A Zahner IM6 potentiostat with a built-in frequency analyzer for electrochemical impedance spectroscopy measurements. The potentiostat had a PP201 20 A booster from Zahner-Elektrik.

Impedance spectra were recorded at open circuit potential (OCP) and at 1.5 V (non-IR corrected) in the frequency range 100000-0.1 Hz. The amplitude was 50 mV. The Nyquist plots were fitted to equivalent circuits using the software Zview 3.4e by Scribner Associates, Inc. The EIS spectra have been modelled using the $LR_s(Q(R_{CT,1}(LR_{CT,2})))$ equivalent circuit as described by Harrington and Conway (41), except that the ideal double layer capacitance, C_{dl}, has been replaced by a constant phase element, Q (or often denoted as CPE). The first resistance in the equivalent circuit denotes the ohmic resistance of the electrolyte including the leads to the electrode, also known as the series resistance, R_s, and the first L is the inductance of external wires. The second and third resistances are the charge transfer resistances of the first and second half spheres in the Nyquist spectra, also denoted as $R_{CT,1}$ and $R_{CT,2}$, respectively. The last L is the inductance associated with adsorbed species, L_{ads}.

The double layer capacitance was approximated by the effective capacitance, C_{eff}, as given by Equation 10 (same as Equation 15 in Orazem et al. (42) developed for Faradaic systems), or alternatively extracted from the imaginary impedance in the high frequency range (100000-5000 Hz).

$$C_{eff} = Q^{\frac{1}{\alpha}} \left(\frac{R_S (R_{CT1} + R_{CT2}}{R_S + R_{CT1} + R_{CT2}} \right)^{\frac{1-\alpha}{\alpha}} \quad 13$$

In Equation 10, α is the dimensionless constant phase element exponent.

The double layer capacitance was also extracted using the high frequency range (100000-5000 Hz) assuming the simple circuit LRC to applies in this region. L represents the inductance of the leads to the cell, R represents the resistance of the electrolyte between the anode and the reference electrode

(including leads to the working electrode) and $C_{dl,\ high\ frequency}$ is the capacitance of the anode. It was assumed that for high frequencies, no or negligible faradaic reactions occur, hence the only contributions to the imaginary impedance are inductance from the external leads and double layer capacitance.

The inductance, L, was extracted from the raw data from EIS at 1.5 V at the highest frequency (100000 Hz) according to Equation 11:

$$L_{100000\ Hz} = \frac{Z_{Im,100000\ Hz}}{2\pi f} \quad (14)$$

In Equation 11, f is the frequency and Z_{Im} is the imaginary impedance. The inductance was then used to calculate the capacitance using Z_{Im} for each frequency step according to Equation 12.

$$C_{dl\ frequency} = \frac{10^6}{1.52 \cdot 2\pi f(2\pi f L - Z_{Im})} \quad (15)$$

$C_{dl,\ frequency}$ was then plotted vs. frequency and from the graph a horizontal capacitance range was found in the high frequency region. This horizontal range was used to determine $C_{dl,\ high\ frequency}$. The method is further described in (43-45).

3. Results and Discussion

Physical Properties and Structure of the Test Anodes

385 Table 2 shows density and air permeability for the anodes used in the study. The 35.0 % and 49.0 %
386 isotropic coke anodes are higher in density than all the other anodes, and in general the air
387 permeability correlates with the density of the anodes, except for the 100 % isotropic coke anode. The
388 high permeability of the 100 % isotropic coke anode is most likely related to a non-optimal packing due
389 to different grain size distribution and/or a too high level of pitch. The chosen pitch level of the pilot
390 anode series was probably too high for the isotropic coke, creating large pores during baking.

391

392 Table 3 shows the sulfuric and metallic impurity levels of the anodes, as determined by XRF. The
393 ultrapure graphite sample was as expected, low in all impurity elements. The anisotropic coke anode
394 (0 %) had a relatively low sulfur content, while the isotropic coke (100 %) anode is high in sulfur and
395 metallic impurities. Since the pitch is the same for all anodes, the increasing impurity content reflects
396 the content of isotropic coke.

397

398 Figure 2 shows the porosity analysis of the anodes vs. pore diameter, as obtained by optical
399 microscopy. The results are the average of two parallels for each anode sample. Graphite was not
400 investigated due to difficulties in getting epoxy to penetrate the very small pore structure. Pores in the
401 30-100 µm range observed for the 7.2 % to 49.0 % isotropic coke anodes are attributed to effects
402 related to packing, as neither the 0 % nor the 100 % anode have significant amounts of pores in this
403 range. The 100 % isotropic coke anode has large pores peaking at 300 µm that are not present in the
404 other anodes. These large pores reflect the non-optimal packing of the coke grains.

405

406 Figure 3 shows a representation of each anode sample investigated by optical microscopy. The entire
407 anode surface area was scanned creating multiple images that were combined into one, allowing the
408 porosity to be measured by contrast differences between the pores and the carbon phase. The red

409 color is the carbon phase, and the yellow color is the epoxy that had penetrated into pores and voids
410 in the sample. The epoxy creates a good contrast between the carbon and the pores. In Figure 3 the
411 larger pores in the 100 % isotropic coke anode are apparent.

412

413 As the optical technique is limited to pores larger than 5-10 µm, the porosity was also measured using
414 Hg porosimetry. Figure 4 shows the differential intrusion of mercury vs. pore size diameter of the
415 anodes. The graphite sample shows very low porosity except in the range between 0.3-1 µm. In the 1-
416 10 µm range the 0-49.0 % anodes show some porosity, while the 100 % anode has very little porosity.
417 For the 0-49.0 % anodes, the fines were purely anisotropic coke as shown in Table 1 and this appears
418 to have a significant effect on the quality of the anode as the coke/pitch interaction depends on the
419 type of coke.

420

421 In general, the results from the Hg porosimetry measurements have peaks at lower pore diameters
422 compared to the results from optical microscopy digital analysis (Figure 2 and Figure 4, respectively).
423 The optical microscopy method is a maximum measuring technique, which measures a pore as the
424 largest circle that can fit into a void filled with epoxy. This gives a more realistic measure of the size of
425 the pores than Hg porosimetry, which records the pressure needed to penetrate the bottleneck of the
426 pore and relates this to the pore size. It provides no information about the size of the pore past the
427 bottleneck. Both methods only measure open porosity. The porosity in the range 10-100 µm in Figure
428 4 is interpreted as related to the quality of the packing between the isotropic and anisotropic coke
429 particles, as the peaks are mainly observed for the mixed anodes. The 49.0 % isotropic coke anode
430 shows a particularly small number of pores in this range, suggesting that the packing between the coke
431 grains for this anode is very good.

432

433 *Electrochemical Characterization*

434 The voltage obtained at 1.0 A/cm^2 for one repeat of each sample in the anode series is shown in Figure
435 5. As has been reported in several other works (14, 17-25), a quasi-periodical dynamic pattern of
436 bubble build-up and release was observed. When introducing isotropic coke, the regularity of the
437 oscillation patterns become irregular and more sawtooth-like, as seen in Figure 5. It should be noted
438 that the voltage oscillations are the response of both surface and solution phenomena and effects of
439 these can therefore not be distinguished from each other. As all experiments have been performed in
440 a similar cell, with the same alumina saturated electrolyte and constant anode geometry, the
441 differences in voltage oscillations are attributed to the differences in electrode. Figure 6 shows a
442 summary of the average of the last 5 voltage oscillation amplitudes for all samples tested during three
443 individual duplicate runs with fresh electrolyte. During each duplicate run one or two repeats were run
444 of each anode sample. In Figure 6b, the average of all the pilot anode samples are shown together with
445 the corresponding standard deviations for 3-5 anodes, except for the 7.2 % isotropic coke anode which
446 was only tested once.

447

448 From Figure 6 it is evident that graphite has much higher voltage oscillation amplitudes than the pilot
449 anodes, and also significantly less bubble noise, indicative of formation of fewer bubbles. A suggested
450 reason for the high potential oscillation amplitudes of graphite is the very dense and nearly polished
451 surface, with a high proportion of very small pores < 1 µm, see Figure 4, acting as nucleation sites. As
452 reported by Cassayre, Utigard and Bouvet (28), many small bubbles were observed at the surface of a
453 graphite anode studied in a see-through cell, which coalesced without escaping, and formed one large
454 bubble screening a large fraction of the surface before it eventually detached. Zhao et al. (18) reported
455 similar findings with larger graphite anodes. These observations are consistent with the graphite
456 voltage oscillations observed in this work. The formation of a high number of smaller bubbles, which
457 coalesce into one large bubble, is seen from the high amplitude of the voltage. The smooth voltage

458 oscillation curve, the high amplitude, and the abrupt drop in voltage is consistent with the growth of
459 bubbles into one large bubble, which screens a high fraction of the surface before it is released.
460 Similarly, the 0 % isotropic coke anode also exhibits less bubble noise and higher amplitudes compared
461 to the anodes with some fraction of isotropic coke, indicative of coalescence of the many smaller
462 bubbles into large bubbles, and limited detachment of bubbles during the oscillation. The bubble
463 oscillations are relatively similar for all the mixed anodes. From the optical images, Figure 2 (pores > 5
464 µm), it should be noted that the pore size distribution is relatively similar for the mixed anodes,
465 whereas the 0 % isotropic coke anode has a peak at a lower pore diameter, and the 100 % isotropic
466 coke anode has a peak at a higher pore diameter. The trends are similar for the same pore diameters
467 obtained by Hg-porosimetry, see Figure 4, but more irregular for the smaller pores (diameter < 10 µm).
468 For the mixed anodes, the oscillations are noisier, indicative of coalescence and formation of multiple
469 bubbles, but also release of bubbles during the growth phase. Due to a lack of regularity in the voltage
470 signal for these anodes, Fast Fourier Transform (FFT) analysis could not be used. Regarding the 100 %
471 isotropic coke anode, the voltage oscillations are irregular and with a low amplitude.

472

473 Figure 7 shows current vs. time response for graphite and the pilot anodes when 2.5 V was applied for
474 200 s. Based on these results, bubble volume and bubble screening on the anode was estimated under
475 the assumption that the anode is free of bubbles when the current density reaches its maximum value.

476

477 Figure 8 shows the calculated average bubble volume for the anodes including graphite, assuming all
478 gas formed is CO_2. Due to the breakdown of the regularity of the voltage oscillations when isotropic
479 coke is blended in, there is some difficulty in determining the time period, Δt, of the oscillation and
480 this is reflected in the relatively high standard deviations for the blended anodes. The high standard
481 deviation for blended anodes is due to the break-down of the regular sawtooth pattern as seen in
482 Figure 5. The bubble volume is relatively similar for all anodes. Compared to the estimated bubble

volumes in (20), the values of the 100 % isotropic coke anode are similar, but the values of the graphite and the 0 % isotropic coke anode are slightly higher, but still within the relatively large standard deviation of the results in (20). The bubble volumes obtained here are also comparable to other results from tests in laboratory cells. Aaberg et al. (19) obtained 0.5-0.6 cm^3/cm^2 for graphite anodes (Ø = 100 mm) in laboratory scale cells. For industrial cells, Houston et al. (46) estimated bubbles to be of size 0.2-0.5 cm^3/cm^2 based on measurements of the bath resistivity for various ACD (anode-cathode distances).

Figure 9 shows the percentage of bubbles covering the anode surface calculated by using the maximum over the minimum current amplitude observed for each anode sample when a constant voltage of 2.5 V was applied. The fraction of the anode surface screened by bubbles ranges from 14-90 %, depending on the anode material in use, and this is in fair agreement with (20). This suggests that bubble screening is highly material dependent. Similar values have previously been obtained with graphite anodes in laboratory experiments, in the range 65-90 % (19), and 70-90 % (18). The very low screening of the 100 % isotropic coke anode, despite the bubbles having similar volumes compared to the other pilot anodes, is probably related to the high porosity of this anode.

As can be seen from Figure 9, graphite has much higher bubble screening than the pilot anodes. From the 14.2 % isotropic coke anode towards the 100 % isotropic coke anode, the bubble screening decreases from 43 % to 14 % and the 35.0-100 % isotropic coke anodes all have lower bubble screening than the 0 % isotropic coke anode. Exactly why the bubble screening for the 14.2 % isotropic coke anode seems to be higher than the 0 % isotropic coke anode is not fully understood, but considering the rather large standard deviation, this may be within experimental uncertainty.

About ~38 % screening of the 0 % isotropic coke anode was found in the present work (Figure 9) compared with ~50 % in Thorne et al. (20). In (20), the size of the anodes is slightly smaller: 8 mm compared to 10 mm in the present work. Although oscillations were found to be similar for 8, 10 and 14 mm graphite anodes, there was a significant effect of size when reducing to 6 mm, as the anode working surface in this case was fully blocked. Such size effects might be slightly different for different materials. Another possible source of error during anode screening experiments may be related to small differences in the horizontal alignment of the anodes. A slightly tilted anode will change the buoyancy effect underneath the anode and hence change the velocity regime for bubble release (19, 47, 48). Furthermore, some inaccuracy may result from the assumption that the anode is free of bubbles at the maximum current.

A viable explanation as to why the bubble screening in general is lower for anodes containing isotropic coke, when bubbles appear to be similar in size upon detachment, is the increased electrolyte wettability for the anodes containing isotropic coke compared to anodes containing anisotropic coke only. Better wetting between anode and electrolyte implies a reduced contact angle, and a correspondingly higher gas-solid contact angle. Cassayre et al. (29) compared graphite anodes and inert (oxide) anodes. The size of the bubbles was found to be considerably smaller for the inert anodes, and thus the blocking of the anode surface was reduced, which was attributed to better wetting between anode and electrolyte.

Wetting Properties of Polarized Anode Samples

To investigate the wetting properties of the anodes in the present work, the in-house designed immersion-emersion wetting technique apparatus, as described in the experimental section and in (32, 33), was used for determination of wetting properties between the anodes and electrolyte before and after polarization. Figure 10 shows examples of the raw data results from steps 1-4 for one of the 0 %

532 isotropic coke anodes. Figure 10a shows steps 1 and 2, which are identical except that in step 1 the
533 sample is a dry, virgin sample that has not been in contact with the electrolyte. As can be seen from
534 the figure, the results from step 1 and 2 are fairly similar.

535

536 Figure 10b shows the immersion-emersion raw data during step 3, where a current of 50 A is applied
537 for 10 s before the emersion. It is evident that the weight of the meniscus (m_σ) is higher in step 3
538 compared with steps 1 and 2 where the sample had not been polarized. Figure 10c shows raw data of
539 step 4. The change in the meniscus length is apparent also in step 4 and this suggests that the change
540 in wetting seen after polarization is permanent due to adsorbed species on the anode surface as
541 suggested by Solheim et al. (33).

542

543 Figure 11 shows corrected weight, m_m-m_t, of the sample during immersion where the weight in gas
544 and the buoyancy effect (m_t) has been subtracted from the recorded weight (m_m) as described in
545 Equation 6. The corrected weight is calculated from the raw data shown in Figure 10c. An arrow in
546 Figure 11 indicates the range where the average m_m-m_t is reported. The negative m_m-m_t value indicate
547 a non-wetting regime between the anode surface and the electrolyte.

548

549 Figure 12 shows a summary of the corrected weight and the calculated wetting angle from Equations 7
550 and 9. The reported values are average m_m-m_t values including one standard deviation of the horizontal
551 region of the immersion as indicated with an arrow in Figure 11. This horizontal region is least affected
552 by electrolyte meniscus build up. It is evident that there is a difference in the wetting conditions
553 between the samples a) before and b) after polarization, and for all samples the wettability of the
554 anode towards the electrolyte is improved after polarization. Wetting appears to increase with
555 increasing isotropic coke content, in particular the samples of 49.0 % and 100 % isotropic coke

demonstrate a significant transition from negative to positive wetting interaction upon polarization. The bubble oscillations (Figure 6) were reduced also for samples containing smaller amounts of isotropic coke. It should be noted, however, that the experiments are quite different, as the voltage oscillations are related to screening of the horizontal anode surface, while the wetting experiments are related to the formation of meniscus on a vertical surface.

The sawtooth like bubble build-up pattern seen especially for the blended anodes in Figure 5, is caused by a reduction in partial surface blocking of the surface before the bubbles are released. This may be explained either by bubbles being released from the anode surface before coalescing, or that the bubbles do coalesce, but screen the anodes less due to the increased wetting observed for the anodes containing isotropic coke.

Surface roughness of the anode during electrolysis

As anodes varied with respect to porosity and permeability, surface roughness was also assessed before and after electrolysis to investigate whether differences in these properties could be associated with the observed differences in voltage oscillations and wetting properties. The surface roughness of the anodes was investigated using confocal microscopy to create contour images of the surfaces before and after electrolysis at 1.0 A/cm^2 for 25 mins. The images in Figure 13 show confocal microscopy contour maps before electrolysis in the left column and confocal microscopy contour maps after electrolysis and after the electrolyte had been removed for the anodes with 0 %, 49.0 % and 100 % isotropic coke content. In the confocal microscopy contour images, the color red denotes "hills in the landscape" and green denotes "valleys in the landscape".

By inspection of the contour images before and after electrolysis in Figure 13a-d, the most pronounced difference in consumption of various coke particles on the anode surface is between coke particles high and low in porosity. Particles high in porosity (so-called "bubble or foam coke") are visible for all anodes containing anisotropic coke (Figure 13a-h) and these coke particles are consumed at a slower rate than the matrix. This is most likely due to a lower electrical conductivity through these grains, alternatively to poorer wetting between electrolyte and anode surface during electrolysis. Similar phenomena were also previously observed by computed tomography before and after electrolysis (49).

For all the anode samples in Figure 13 increased consumption can be seen for the binder matrix between larger coke grains. Previous works have found increased CO_2 reactivity for binder phase compared with larger coke grains, and many have therefore suggested that pitch is more reactive than coke during electrolysis (3, 6, 43, 50, 51). The contour surface map images before and after electrolysis support these findings. For the 49.0 % isotropic coke anode samples (Figure 13e-h) no significant difference in consumption between isotropic and anisotropic coke grains is observed (apart from the so-called "bubble grains").

Figure 14 shows true area (TA) over projected area (PA) for the entire series of anodes varying in isotropic coke content before and after electrolysis. An increase of 30-50 % in surface area is observed for the electrolyzed sample compared with the fresh, ground anode sample. This is in good agreement with the EIS measurements performed by Thonstad, where he observed an increase in surface area of 45 % (51). The two anodes with the least surface roughness (35.0 % and 49.0 % isotropic coke content) are also the two anodes with the highest density/lowest porosity.

603 The surface roughness on the anodes was also investigated during electrolysis by electrochemical
604 impedance spectroscopy. Nyquist plots with impedance raw data and modelled data with equivalent
605 electrical circuit LR(Q(R(LR))) are shown for one parallel measurement of each anode, in Figure 15. Two
606 parallel anodes were investigated per duplicate run, and two consecutive runs with fresh electrolyte
607 and reference electrodes were performed. The impedance data were recorded at 1.5 V (non-IR
608 corrected value). From Figure 15, an inductive loop at the lower frequencies can be seen. This is
609 attributed to the charge transfer mechanisms as described in e.g. Equations 2 and 3, typical for
610 adsorbed intermediate species. The vertical part of the curve at high frequencies (indicated in Figure
611 15) was used to extract the double layer capacitance from the LRC-circuit. In this frequency range it is
612 assumed that no Faradaic reactions take place, only adsorption/desorption reactions. Since these
613 experiments were run in an electrolyte saturated in Al_2O_3 it is assumed that the concentration
614 overpotential is negligible and that the diffusion double layer is small. Hence, the reaction is assumed
615 to be charge transfer controlled. In the Supplementary material added to this article, Tables S1 and S2
616 show the parameters obtained when modelling the impedance raw data with the equivalent electrical
617 circuit LR(Q(R(LR))) for the first parallel for the two duplicate runs, respectively. These parameters
618 include inductance, L, series resistance, R_s, constant phase element, Q, the dimensionless constant
619 phase element exponent, α, resistance to charge transfer, $R_{CT,1}$ and $R_{CT,2}$, and inductance of adsorbed
620 species on the electrode surface. One source of variation in results between the two consecutive runs
621 is that the current density varies between runs when taking the IR-drop into consideration. The
622 variation in current density will also affect the resistance to charge transfer, R_{CT1}, as can be seen in
623 Tables S1 and S2 in the Supplementary material. The reason for this variation in current density is due
624 to small production differences in the in-house produced reference electrodes between runs and their
625 position in the electrolyte between the runs.

626

627 Figure 16a shows average effective capacitance, C_{eff} (n = 4), and double layer capacitance at high
628 frequency, $C_{dl,\ high\ frequency}$ (n=4), for all parallel anodes for the two duplicate runs. The effective
629 capacitance was calculated using Equation 10 and parameters given in the Supplementary material.
630 The high frequency double layer capacitance was calculated using the LRC circuit at high frequencies,
631 and the values are comparable to the values for C_{eff} for all the anodes. The values for the capacitances
632 are within the ranges reported previously by Thonstad (43), and slightly lower than that reported
633 elsewhere (9, 44, 50, 52).

634

635 The capacitances are similar for the 0 %-35.0 % isotropic coke anodes within the standard deviations
636 given. However, from Figure 16a it is evident that both the 49.0 % and 100 % isotropic coke anodes
637 show a higher capacitance than the remaining pilot anode series. The capacitance values were
638 corrected for real surface area obtained by confocal microscopy (*cf.* Figure 14) in order to verify that
639 the capacitance difference seen for the 49.0 % and 100 % isotropic coke anodes are not merely due to
640 real area differences after electrolysis. Figure 16b shows capacitance over true area/projected area vs.
641 isotropic coke content after electrolysis. An increase in capacitance is still observed after correction
642 for the ratio of true area over projected area. This implies that the capacitance increase seen for the
643 49.0 % and 100 % isotropic coke anodes, but also to a certain extent the 35.0 % isotropic coke anode,
644 are due to a difference in surface wetting properties of these anodes towards the electrolyte as was
645 found in Figure 12b.

646

647 From the wetting results shown in Figure 12, the samples with 49.0 % and 100 % isotropic coke show
648 improved wetting properties compared to the samples with less or no isotropic coke. These samples
649 are very different to each other with respect to surface roughness, excluding effects of surface
650 topography on the measured wetting of the samples. Similarly, the development of surface roughness
651 during electrolysis, as shown in Figure 14, appears to be independent of the anode material.

Altogether, the results from the wetting experiments performed under polarized conditions, and electrochemical measurements of voltage oscillations and capacitance, provide evidence of improved wetting towards the electrolyte for the anodes with a high content of isotropic coke. The exact reason for these observed differences is not known and are beyond the scope of this study. A more detailed investigation of the material properties is provided in a previous work (53), and this showed that the anisotropic coke had a higher ratio of basal surface planes as well as lower amount of surface oxides (0.02 g/m^2 for the anisotropic coke and 0.035 g/m^2 for the isotropic coke). These material property differences observed in the coke may provide an explanation to the observed differences in electrochemical behavior and wetting properties of the anodes.

The results obtained in this work indicate that there might be benefits from introducing isotropic cokes in industrial scale cells with respect to a reduction of the cell voltage/voltage oscillation amplitude. As some phenomena in industrial scale cells, like the flow patterns, and the size of the anodes cannot be reconstructed in laboratory scale experiments, the effect of the improved wetting will have to be verified in industrial scale cells. Further work in the laboratory could be to repeat the tests with larger anodes made with larger coke grains and a non-saturated electrolyte closer to industrial type. A see-through cell can help investigate the bubble layer thickness on the anodes and give a visual insight in what the bubble build-up and release look like on anodes containing isotropic coke vs. anodes made from pure anisotropic coke.

4. Conclusion

Introduction of unconventional isotropic coke, traditionally categorized as fuel grade coke, into carbon anodes has been shown to have positive effects on the amplitude of potential oscillations and on bubble screening of the anode surface in a laboratory cell with pilot anodes made from 0-2 mm aggregate. In this work, various amounts of isotropic coke were blended into anisotropic coke and the

very periodical voltage oscillation seen for both graphite and the pure anisotropic coke broke down. The bubble build-up pattern became more sawtooth-like, indicating a more irregular growth and release of bubbles. The variation in the observed potential oscillation amplitudes and the degree of bubble screening of the anodes in the test series was attributed to better wettability during polarization, towards the cryolite melt for the anodes containing isotropic coke. The improved wettability between anode and electrolyte was evident both from the immersion-emersion experiments for polarized samples and from the capacitance corrected for surface roughness. As the potential oscillations are reduced with only a small amount of isotropic coke blended in with a traditional anisotropic coke, potential energy savings can be obtained by the additions of isotropic coke in the anodes, provided that these preliminary laboratory results can be confirmed in full scale operation.

Acknowledgement

The work was financed by Hydro Aluminium and The Research Council of Norway through the research program called "HAL Ultra Performance Aluminium Cell". Aksel Alstad at the NTNU workshop is gratefully acknowledged for fabricating the experimental parts. Technicians at Hydro Aluminium Årdalstangen and Jannicke Kvello at SINTEF also deserve a thank you for help with various experimental techniques.

References

1. L. Edwards, F. Vogt, M. Robinette, R. Love, A. Ross, M. McClung, R. Roush and W. Morgan, in *Light Metals 2009*, G. Bearne Editor, p. 985, The Minerals, Metals & Materials Society, Warrendale, PA (2009).
2. L. Edwards, N. Backhouse, H. Darmstadt and M.-J. Dion, in *Light Metals 2012*, C. E. Suarez Editor, p. 1207, John Wiley & Sons, Inc., Hoboken, NJ (2012).
3. K. Grjotheim and H. Kvande, *Introduction to Aluminium Electrolysis: Understanding the Hall-Heroult Process*, Aluminium-Verlag, Düsseldorf (1993).
4. F. Nordmo and J. Thonstad, *Electrochim. Acta*, **30**, 741 (1985).
5. J. Thonstad, *J. Electrochem. Soc.*, **111**, 959 (1964).
6. J. Thonstad, P. Fellner, G. M. Haarberg, J. Hives, H. Kvande and A. Sterten, *Aluminium Electrolysis: Fundamentals of the Hall-Héroult Process*, Aluminium-Verlag GmbH, Dusseldorf (2001).
7. G. S. Picard, E. C. Prat, Y. J. Bertaud and M. J. Leroy, in *Light Metals 1987*, p. 507, The Metallurgical Society of AIME, Warrendale, PA (1987).
8. Å. Sterten, *Electrochimica Acta*, **25**, 1673 (1980).
9. A. Kisza, J. Thonstad and T. Eidet, *J. Electrochem. Soc.*, **143**, 1840 (1996).
10. M. A. Cooksey, M. P. Taylor and J. J. J. Chen, *JOM*, **60**, 51 (2008).
11. J. A. Leistra and P. J. Sides, *Electrochim. Acta*, **33**, 1761 (1988).
12. N. E. Richards, in *Light Metals 1998*, B. Welch Editor, p. 521, The Minerals, Metals & Materials Society, Warrendale, PA (1998).
13. S. F. Jones, G. M. Evans and K. P. Galvin, *Adv. Colloid Interface Sci.*, **80**, 27 (1999).
14. K. E. Einarsrud, A Treatise on Interpolar Transport Phenomena, in, Norwegian University of Science and Technology, Trondheim, Norway (2012).
15. L. I. Kiss and S. Poncsak, in *Light Metals 2002*, W. Schneider Editor, p. 217, The Minerals, Metals & Materials Society, Warrendale, PA (2002).
16. J. Zoric and A. Solheim, *J. Appl. Electrochem.*, **30**, 787 (2000).
17. J. Xue and H. A. Øye, in *Light Metals 1995*, J. Evans Editor, p. 265, The Minerals, Metals & Materials Society, Warrendale, PA (1995).
18. Z. Zhao, Z. Wang, B. Gao, Y. Feng, Z. Shi and X. Hu, in *Light Metals 2015*, M. Hyland Editor, p. 801, John Wiley & Sons, Inc., Hoboken, NJ (2015).
19. R. J. Aaberg, V. Ranum, K. Williamson and B. J. Welch, in *Light Metals 1997*, R. Huglen Editor, p. 341, The Minerals, Metals & Materials Society, Warrendale, PA (1997).
20. R. J. Thorne, C. Sommerseth, A. P. Ratvik, S. Rørvik, E. Sandnes, L. P. Lossius, H. Linga and A. M. Svensson, *J. Electrochem. Soc.*, **162**, E104 (2015).
21. K. E. Einarsrud, I. Eick, P. J. Witt, A. Solheim and Y. Feng, in *Light Metals 2015*, M. Hyland Editor, p. 649, John Wiley & Sons, Inc., Hoboken, NJ (2015).
22. K. E. Einarsrud and S. T. Johansen, *Prog. Comput. Fluid Dyn.*, **12**, 119 (2012).
23. Z. Wang, B. Gao, H. Li, Z. Shi, X. Lu and Z. Qiu, in *Light Metals 2006*, T. J. Galloway Editor, p. 463, The Minerals, Metals & Materials Society, Warrendale, PA (2006).
24. B. Gao, X. Hu, J. Xu, Z. Shi, Z. Wang and Z. Qiu, in *Light Metals 2006*, T. J. Galloway Editor, p. 467, The Minerals, Metals & Materials Society, Warrendale, PA (2006).
25. R. Dorin and E. J. Frazer, *J. Appl. Electrochem.*, **23**, 933 (1993).
26. K. E. Einarsrud and E. Sandnes, in *Light Metals 2011*, S. J. Lindsay Editor, p. 555, John Wiley & Sons, Inc., Hoboken, NJ (2011).
27. Z. Zhao, B. Gao, Y. Feng, Y. Huang, Z. Wang, Z. Shi and X. Hu, *JOM*, **69**, 281 (2017).
28. L. Cassayre, T. A. Utigard and S. Bouvet, *JOM*, **54**, 41 (2002).
29. L. Cassayre, G. Plascencia, T. Marin, S. Fan and T. A. Utigard, in *Light Metals 2006*, T. J. Galloway Editor, The Minerals, Metals & Materials Society, Warrendale, PA (2006).
30. E. W. Dewing, *Can. Metall. Q.*, **30**, 153 (1991).
31. D. Kasherman and M. Skyllas-Kazacos, *J. of Appl. Electrochem.*, **21**, 716 (1991).

745 32. A. M. Martinez, O. Paulsen, A. Solheim, H. Gudbrandsen and I. Eick, in *Light Metals 2015*, p.
746 665, John Wiley & Sons, Inc., Hoboken, NJ (2015).
747 33. A. Solheim, H. Gudbrandsen, A. M. Martinez, K. E. Einarsrud and I. Eick, in *Light Metals 2015*,
748 M. Hyland Editor, p. 671, John Wiley & Sons, Inc., Hoboken, NJ (2015).
749 34. I. O. f. Standardization, ISO 5940-2:2007, in *Carbonaceous materials used in the production of*
750 *aluminium -- Pitch for electrodes -- Part 2: Determination of the softening point (Mettler softening point*
751 *method)*, p. 8, International Organization for Standardization (2007).
752 35. I. O. f. Standardization, ISO 6791:1981, in *Carbonaceous materials for the production of*
753 *aluminium -- Pitch for electrodes -- Determination of contents of quinoline-insoluble material*, p. 3,
754 International Organization for Standardization (1981).
755 36. I. O. f. Standardization, ISO 12985-1:2000, in *Carbonaceous materials used in the production of*
756 *aluminium -- Baked anodes and cathode blocks -- Part 1: Determination of apparent density using a*
757 *dimensions method*, International Organization for Standardization (2000).
758 37. I. O. f. Standardization, ISO 15906:2007, in *Carbonaceous materials for the production of*
759 *aluminium -- Baked anodes -- Determination of the air permeability*, p. 7, International Organization
760 for Standardization (2007).
761 38. I. O. f. Standardization, ISO 12980:2000, in *Carbonaceous materials used in the production of*
762 *aluminium -- Green coke and calcined coke for electrodes -- Analysis using an X-ray fluorescence*
763 *method*, p. 9, International Organization for Standardization (2000).
764 39. S. Rørvik and H. A. Øye, in *Light Metals 1996*, W. Hale Editor, p. 561, The Minerals, Metals &
765 Materials Society, Warrendale, PA (1996).
766 40. R. Fernandez and T. Østvold, *Acta Chem. Scandinavica*, **43**, 151 (1989).
767 41. D. A. Harrington and B. E. Conway, *Electrochim. Acta*, **32**, 1703 (1987).
768 42. M. E. Orazem, I. Frateur, B. Tribollet, V. Vivier, S. Marcelin, N. Pébère, A. L. Bunge, E. A. White,
769 D. P. Riemer and M. Musiani, *J. Electrochem. Soc.*, **160**, C215 (2013).
770 43. J. Thonstad, *Electrochim. Acta*, **15**, 1581 (1970).
771 44. S. Jarek and J. Thonstad, *J. Appl. Electrochem.*, **17**, 1203 (1987).
772 45. W. Gebarowski, C. Sommerseth, A. P. Ratvik, E. Sandnes, L. P. Lossius, H. Linga and A. M.
773 Svensson, in *Light Metals 2016*, E. Williams Editor, p. 883, John Wiley & Sons, Inc., Hoboken, NJ (2016).
774 46. G. J. Houston, M. P. Taylor, D. J. Williams and K. Grjotheim, in *Light Metals 1988*, L. G. Boxall
775 Editor, p. 641, Metallurgical Society of AIME, Warrendale, PA (1988).
776 47. S. Fortin, M. Gerhardt and A. J. Gesing, in *Light Metals 1984*, J. P. McGeer Editor, p. 721,
777 Metallurgical Society of AIME, Warrendale, PA (1984).
778 48. A. Solheim, S. T. Johansen, S. Rolseth and J. Thonstad, *J. Appl. Electrochem.*, **19**, 703 (1989).
779 49. C. Sommerseth, R. J. Thorne, S. Rørvik, E. Sandnes, A. P. Ratvik, L. P. Lossius, H. Linga and A. M.
780 Svensson, in *Light Metals 2015*, M. Hyland Editor, p. 1141, John Wiley & Sons, Inc., Hoboken, NJ (2015).
781 50. S. Jarek and J. Thonstad, in *Light Metals 1987*, R. D. Zabreznik Editor, p. 399, The Metallurgical
782 Society of AIME, Warrendale, PA (1987).
783 51. J. Thonstad, *J. Appl. Electrochem.*, **3**, 315 (1973).
784 52. S. Jarek and Z. Orman, *Electrochim. Acta*, **30**, 341 (1985).
785 53. R. J. Thorne, C. Sommerseth, A. P. Ratvik, S. Rørvik, E. Sandnes, L. P. Lossius, H. Linga and A. M.
786 Svensson, *J. Electrochem. Soc.*, **162**, E296 (2015).

787

788

789

790 *Table 1*

Anode name	Coke type	0-1 mm aggregate wt%	1-2 mm aggregate wt%	Fines (< 63 µm) wt%	Pitch content wt%
0 %	A	35.0	38.0	27.0	15.0
	I	0	0	0	
7.2 %	A	32.4	32.4	28.0	14.0
	I	3.6	3.6	0	
14.2 %	A	28.0	28.8	29.0	14.0
	I	7.0	7.2	0	
35.0 %	A	17.5	17.5	30.0	14.0
	I	17.5	17.5	0	
49.0 %	A	10.5	10.5	30.0	14.0
	I	24.5	24.5	0	
100 %	A	0	0	0	15.0
	I	35.0	35.0	27.0	

791

792

793 *Table 2*

Anode name	Density g/cm^3	Air permeability nPm
Graphite	1.771	0.2
0 %	1.603	0.8
7.2 %	1.597	1.1
14.2 %	1.595	1.5
35.0 %	1.651	0.9
49.0 %	1.674	0.6
100 %	1.596	6.9*

*value corresponding to maximum measurable level of the equipment.

794

795

796

797 *Table 3*

Anode name	Na ppm	Si ppm	P ppm	S %	Ca ppm	V ppm	Fe ppm	Ni ppm	Zn ppm	Pb ppm
Graphite	10	10	1	0.00	11	1	25	3	1	1
0 %	56	108	11	0.94	25	70	287	45	5	7
100 %	115	284	4	4.45	227	883	393	372	38	20

798

799

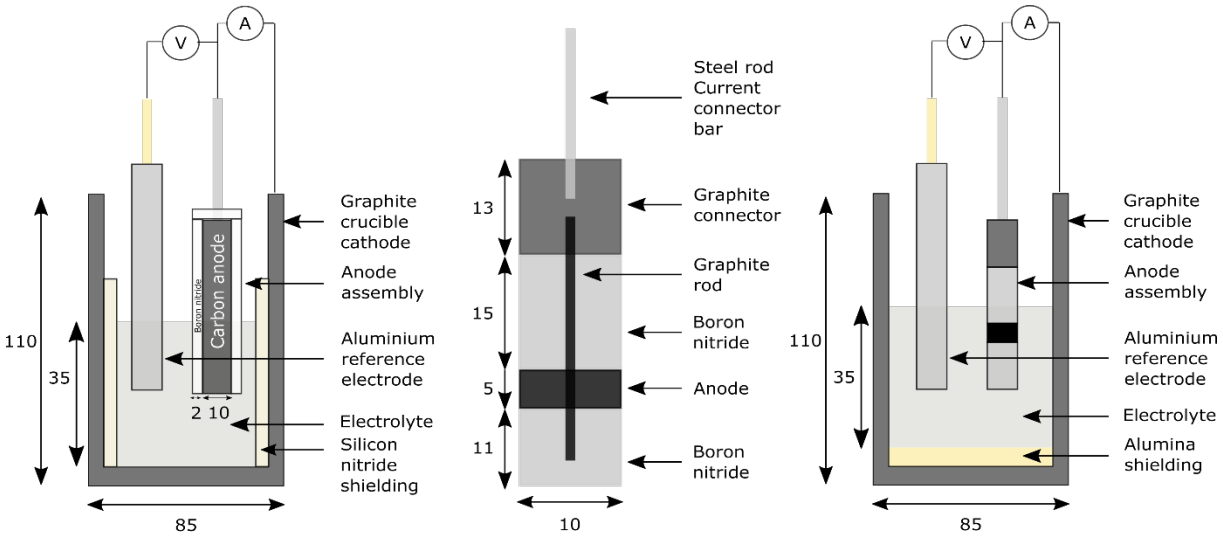

800

801 *Figure 1*

802

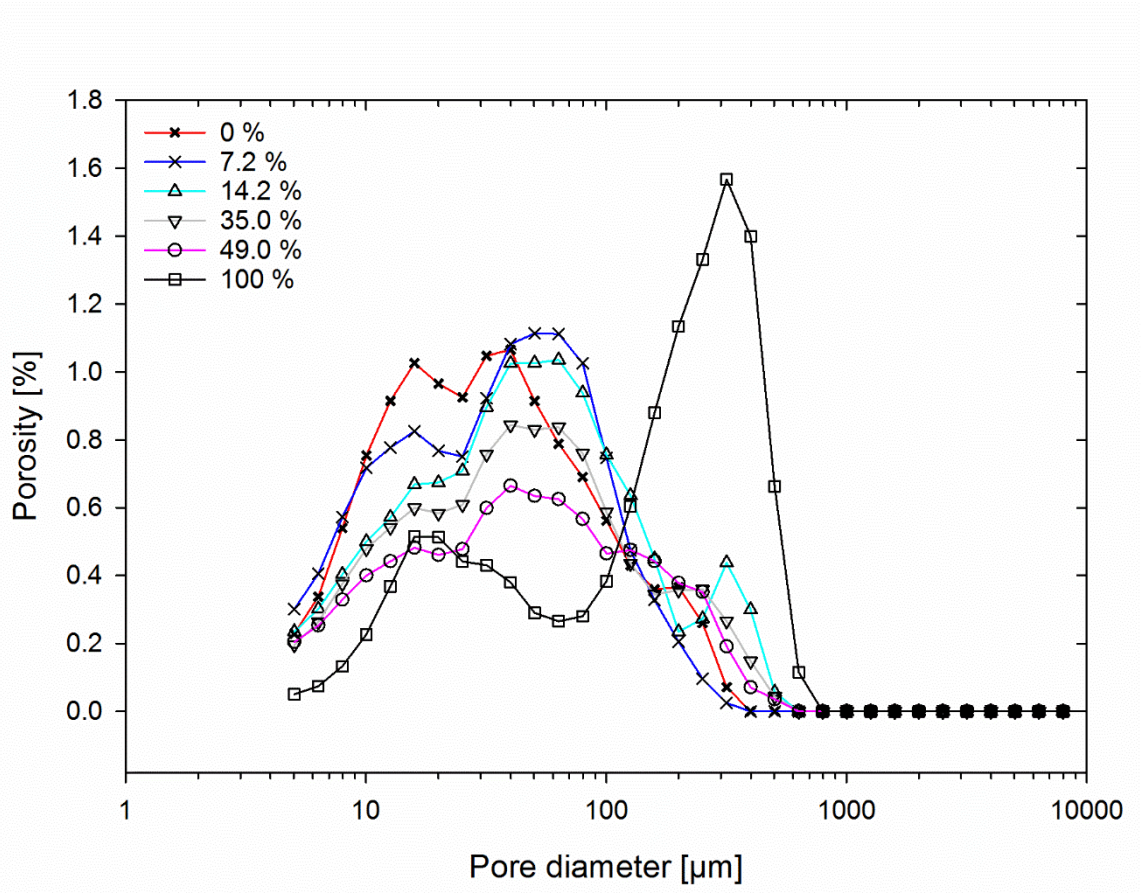

803

804 *Figure 2*

805

806 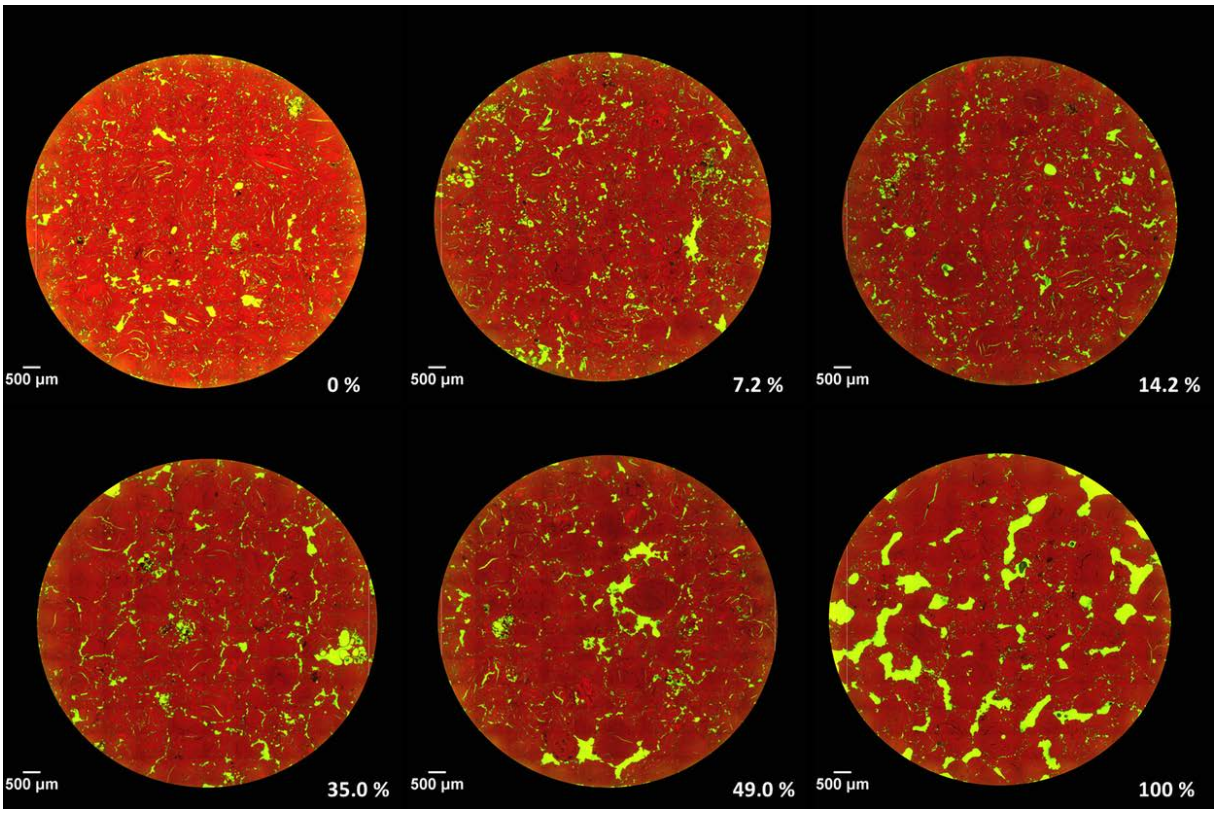

807 *Figure 3*

808

809

810

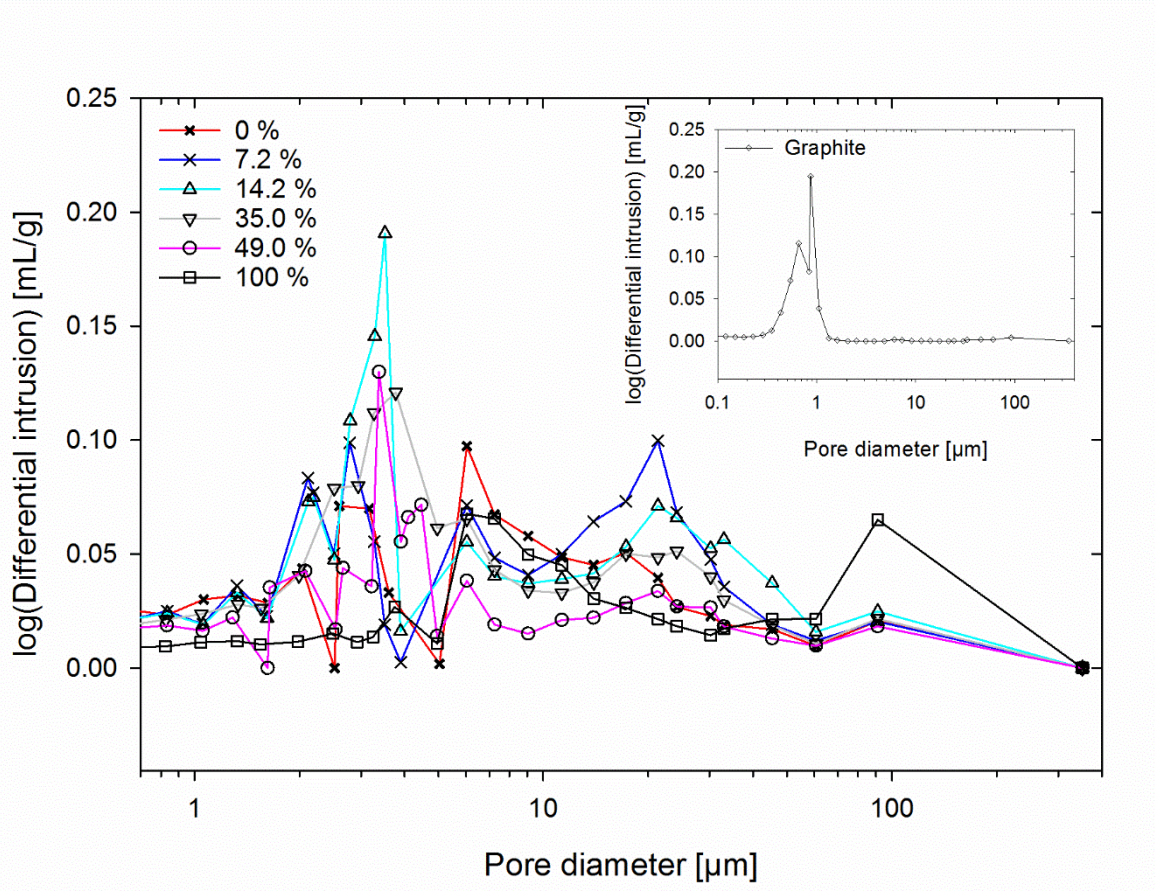
0 %
7.2 %
14.2 %
35.0 %
49.0 %
100 %
log(Differential intrusion) [mL/g]
Pore diameter [µm]
Graphite
log(Differential intrusion) [mL/g]
Pore diameter [µm]

Figure 4

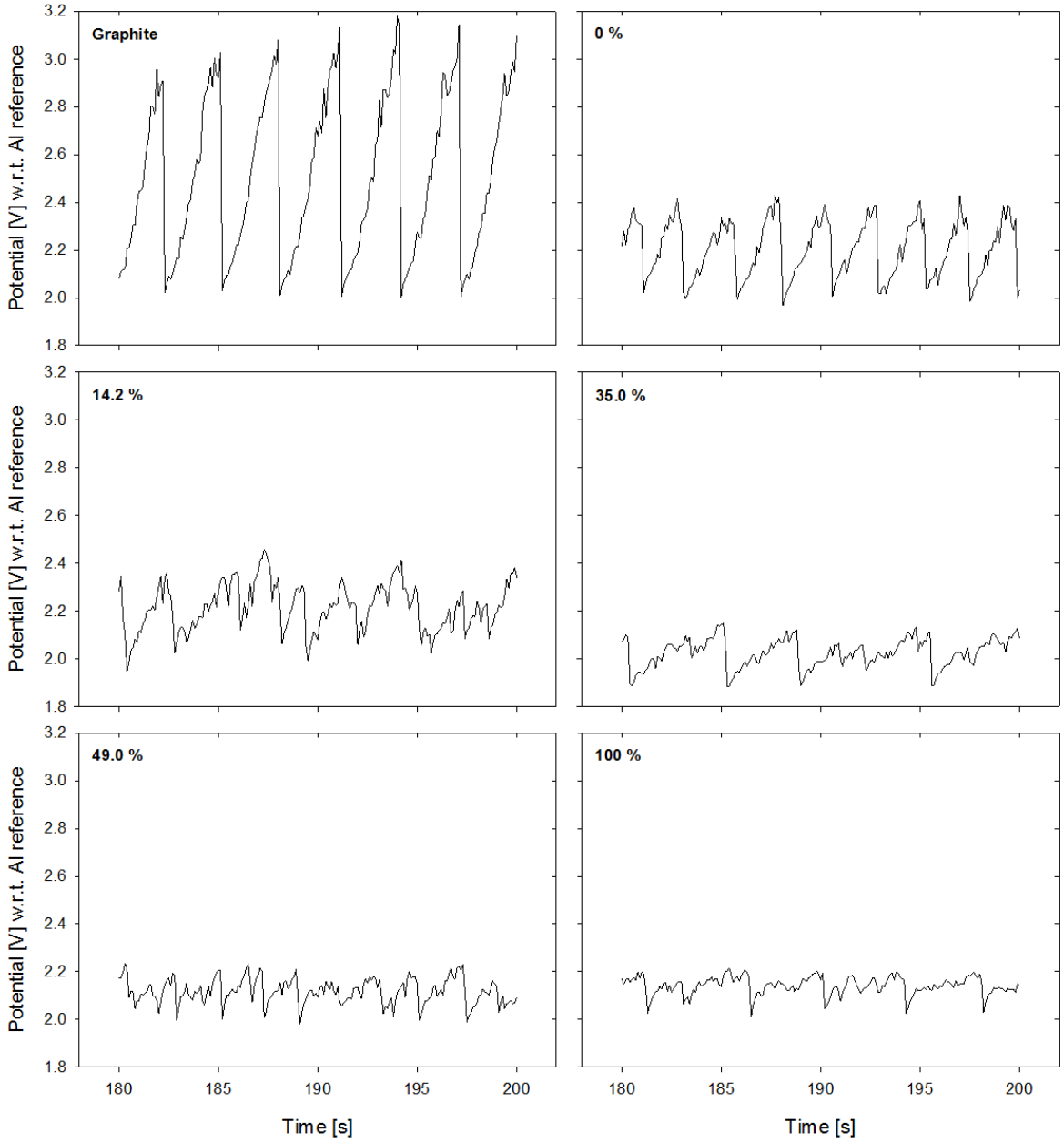

815

816 *Figure 5*

817

818

819

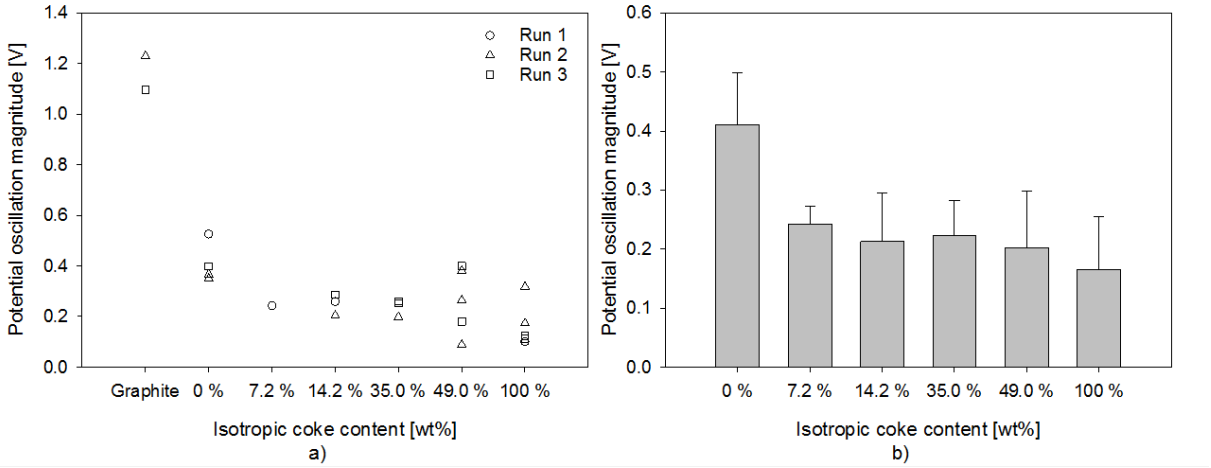

820

821 *Figure 6*

822

823

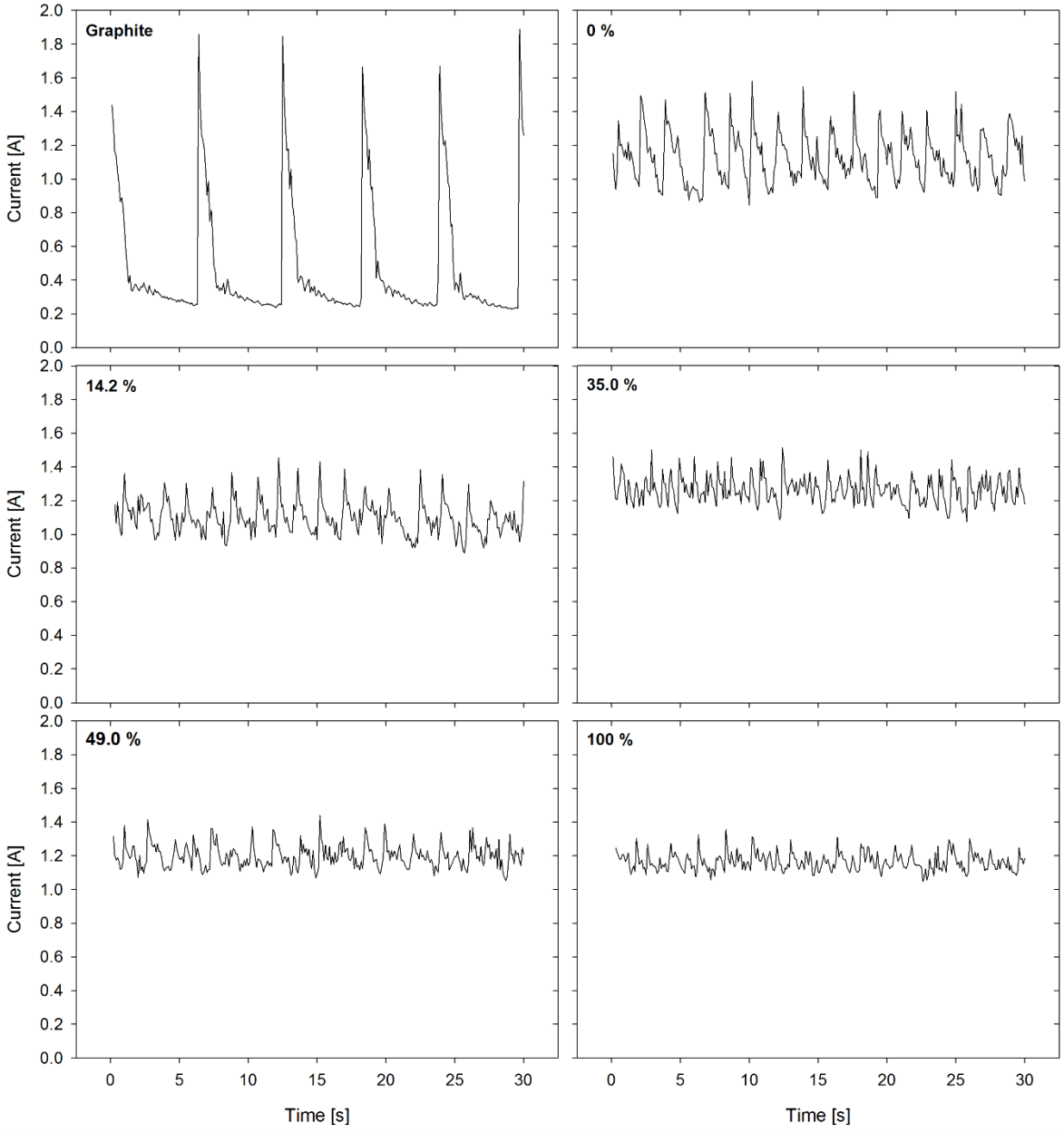

824

825 *Figure 7*

826

827

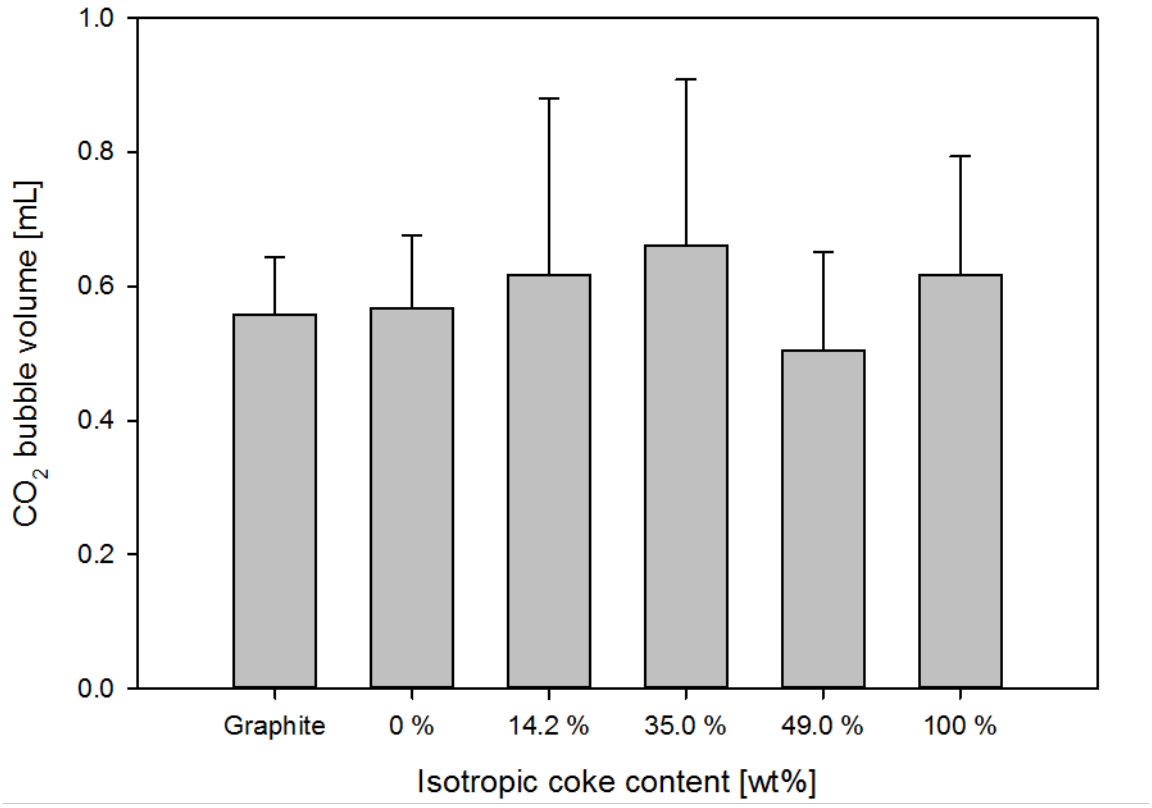

828

829 *Figure 8*

830

831

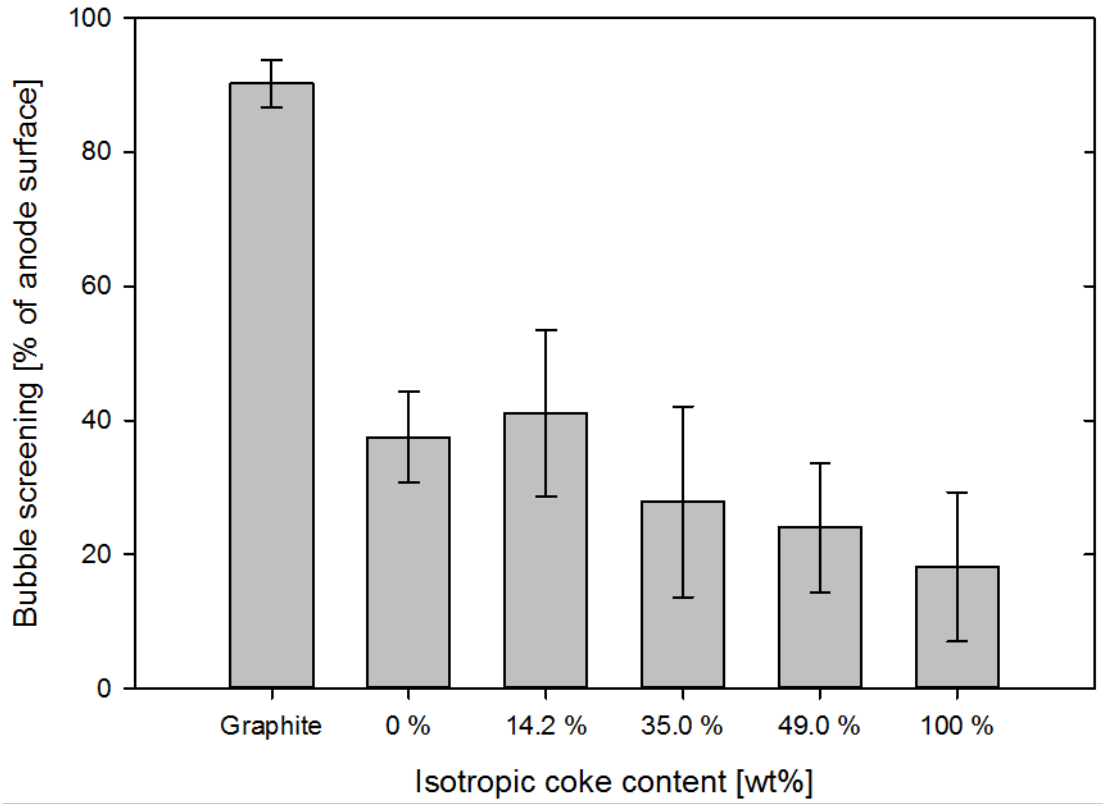

832

833 *Figure 9*

834

835

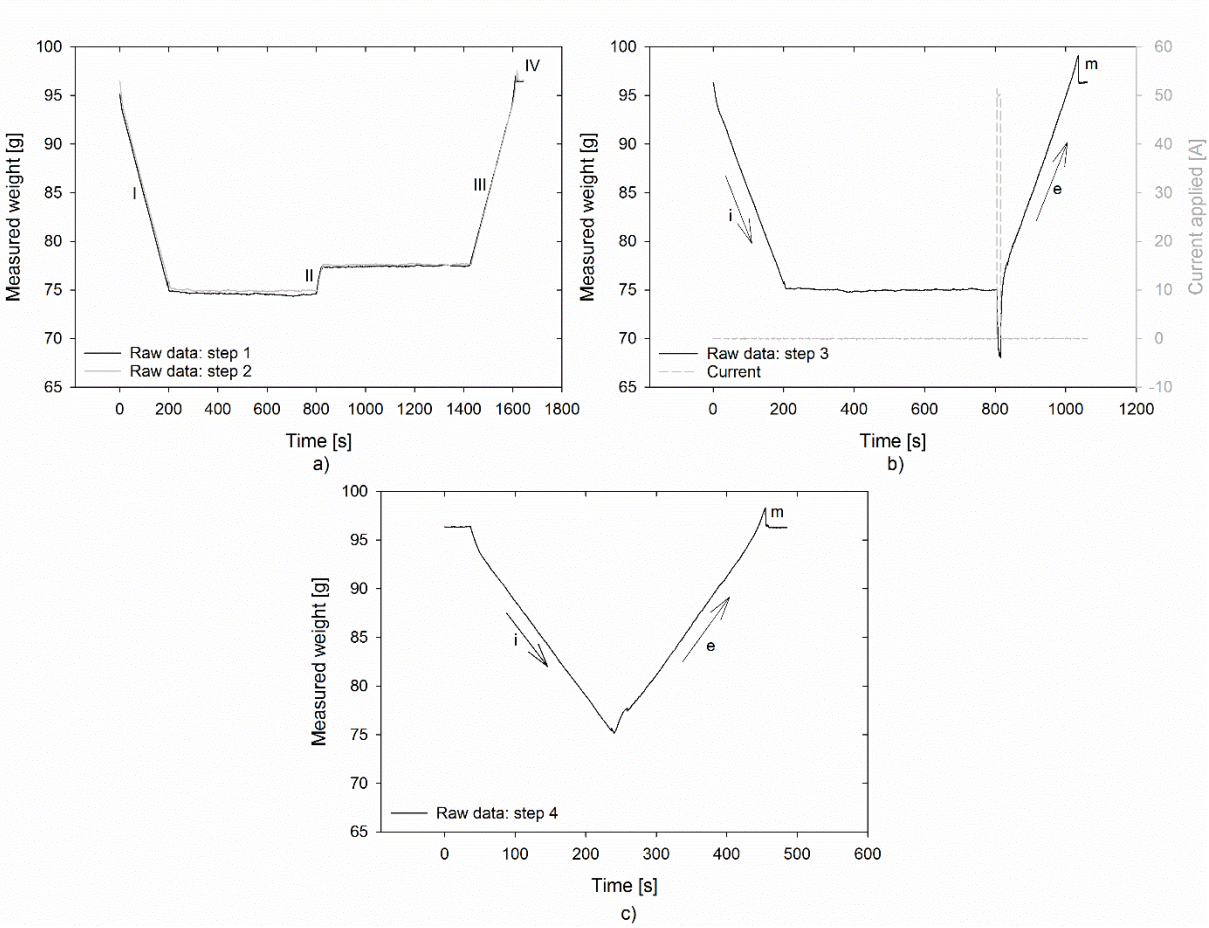

836

837 *Figure 10*

838

839

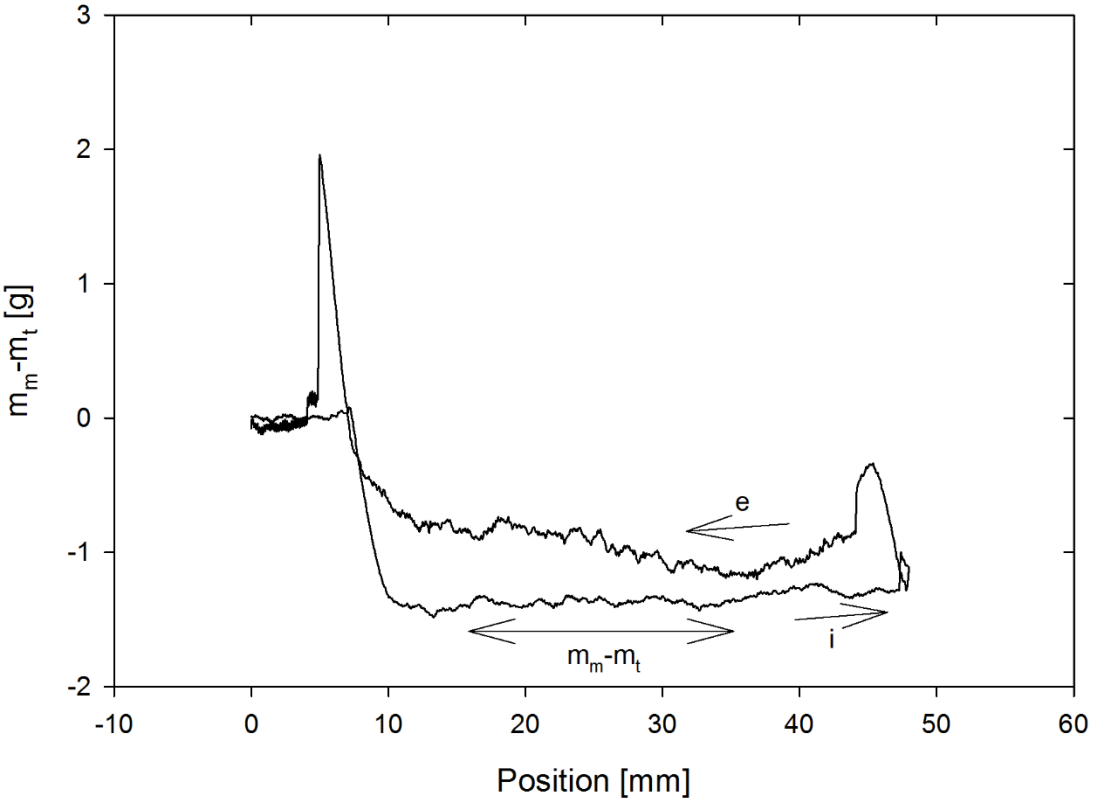

840

841 *Figure 11*

842

843

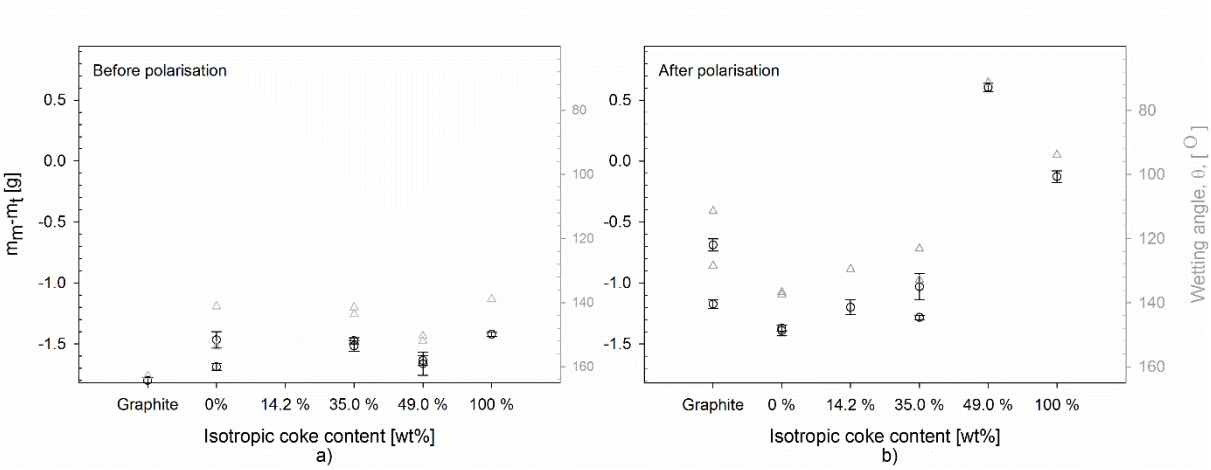

844

845 *Figure 12*

846

847

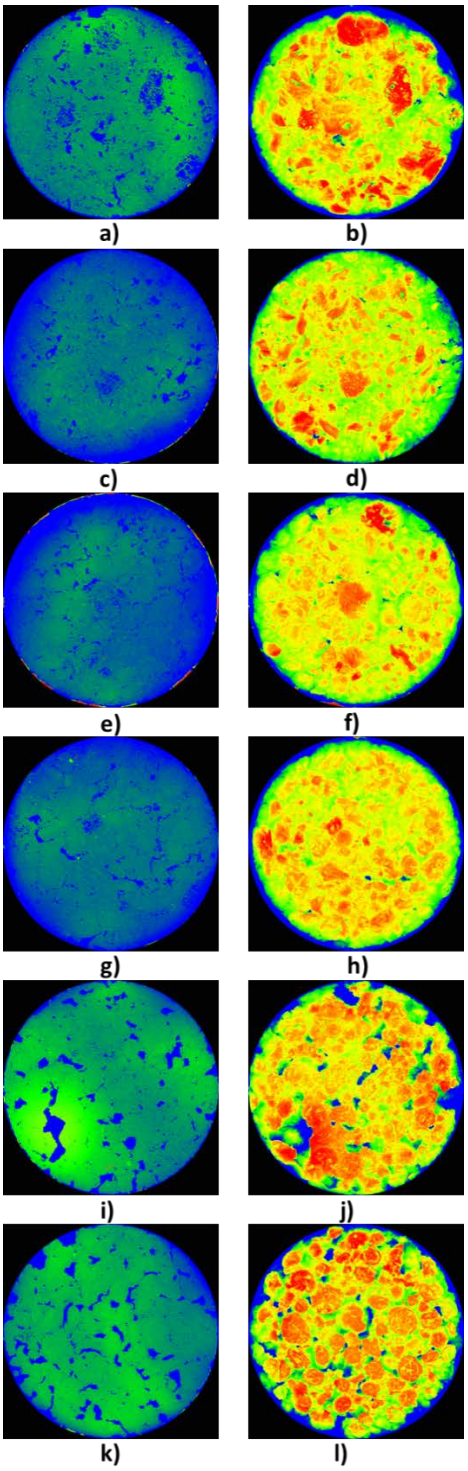

Figure 13

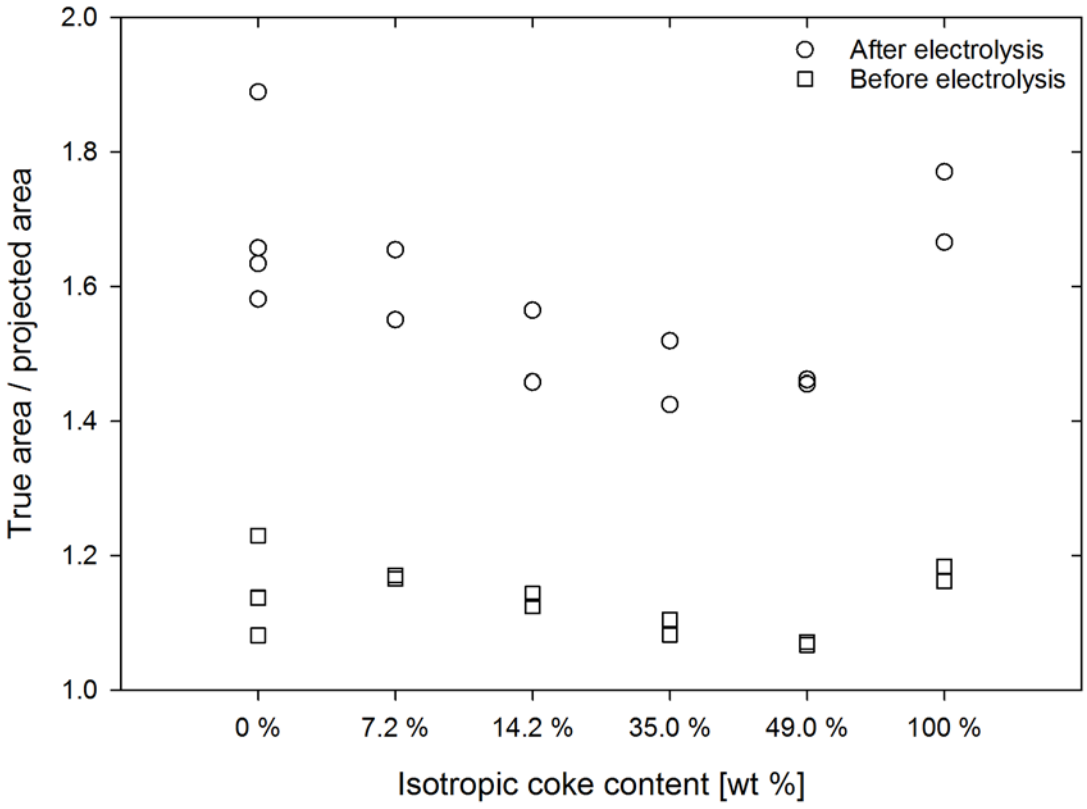

852

853 *Figure 14*

854

855

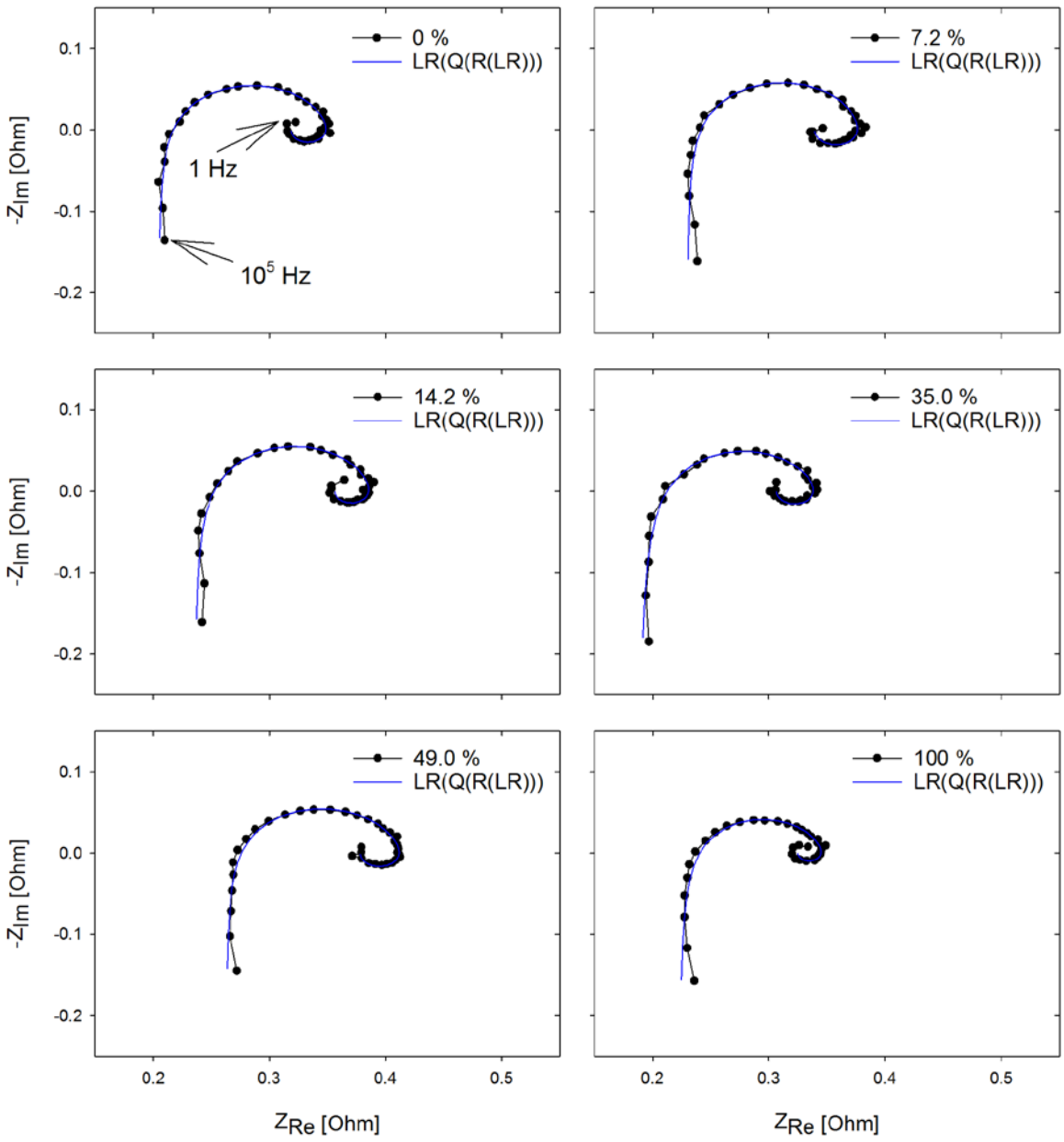

856

857 *Figure 15*

858

859

860 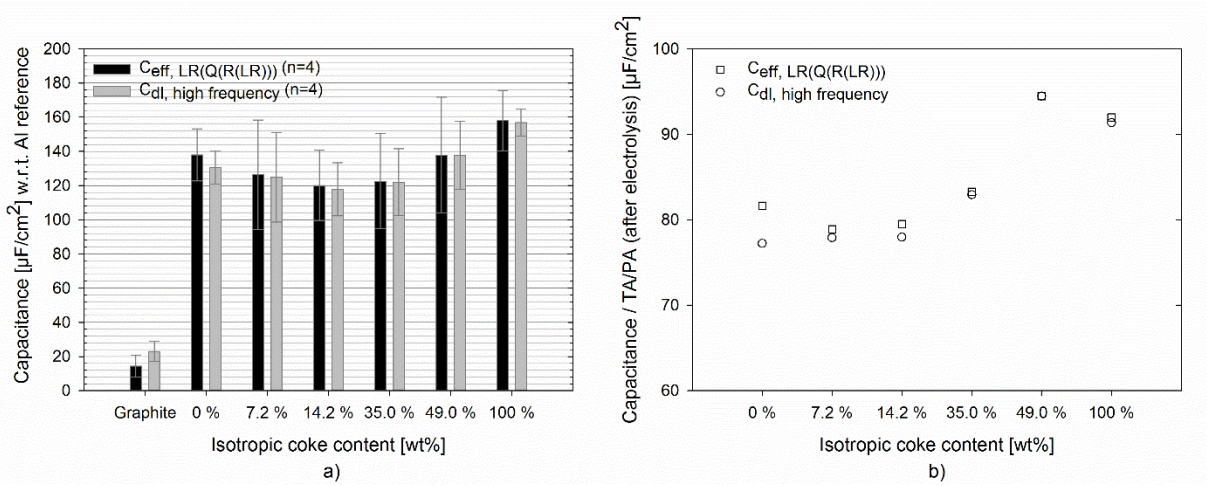

861 *Figure 16*

862

863

Table captions

Table 1. *Pilot anodes. Under coke type, A and I denote anisotropic and isotropic coke, respectively.*

Table 2. *Density and permeability of the anodes. The percentage indicates the amount of isotropic coke in each anode.*

Table 3. *XRF elemental results for graphite and the baked 0 % and 100 % isotropic coke anodes.*

872 **Figure captions**

873 ***Figure 1.*** *a) The horizontal electrochemical laboratory setup used when investigating the bubble build-*
874 *up and release of the different carbon anode materials. b) and c) are sketches of the electrochemical*
875 *setup used for electrical impedance spectroscopy. b) Vertical anode assembly. c) Principle sketch of the*
876 *electrolysis cell used with the aluminum reference electrode, the graphite crucible acting as the*
877 *cathode, the vertical anode assembly and the electrolyte. All measures are in mm.*

878

879 ***Figure 2.*** *Porosity [%] vs. diameter of pores obtained by optical microscopy, averaged from two*
880 *duplicate runs of each sample.*

881

882 ***Figure 3.*** *Optical microscopy images showing pores (yellow) in the different anode materials.*

883

884 ***Figure 4.*** *Differential intrusion of mercury into pores vs. pore size diameter. Note that the scale of the*
885 *x-axis is different between the graphite sample and the anode samples.*

886

887 ***Figure 5.*** *Example of potential vs. time measurements for graphite and the pilot anodes where*
888 *1.0 A/cm^2 was applied for 200 seconds. The last 20 seconds of the 200 s long measurements are shown.*

889

890 ***Figure 6.*** *Potential oscillation magnitude of bubbles evolved during electrolysis at 1.0 A/cm^2 of anodes*
891 *varying in isotropic coke content. a) All results including graphite from three duplicate runs. b) Average*
892 *results with error bars for all anodes except graphite.*

893

Figure 7. *Example of current vs. time for graphite and the pilot anodes where 2.5 V was applied for 200 seconds. The first 30 seconds of the 200 s long measurements are shown.*

Figure 8. *Average bubble volume per bubble evolved during electrolysis at 1.0 A/cm^2 with error bars. For graphite n = 2 and for the remaining anodes, n = 3-5. For each sample the average of 5 bubbles are reported and included in the calculations.*

Figure 9. *Percent of anode surface screened/covered by bubbles calculated from maximum and minimum current measured at constant voltage of 2.5 V. Error bars show one standard deviation, where n=2-5.*

Figure 10. *Example of raw data results during wetting testing of a 0 % pilot anode. a) Step 1 (black) and step 2 (grey). I. is immersion of the sample 40 mm into the electrolyte, II. is the changing the electrolyte height relative to the anode sample to 35 mm, III. is the emersion of the sample and IV. the observed meniscus that appear when pulling the sample completely out of the electrolyte. b) Step 3 (black) and current vs. time (grey). c) Step 4. In b) and c) i=immersion, e=emersion and m=meniscus.*

Figure 11. *The recorded weight (m_m) subtracted with theoretical weight (m_t) vs. the position of the anode sample in the electrolyte for step 4. The part of the graph during immersion that has been used to report average m_m-m_t for the anode samples is indicated. i=immersion, e=emersion.*

Figure 12. *Average m_m-m_t during immersion in Step 4 of the carbon samples into the electrolyte after polarization at 0.7 A/cm^2 (50 A) (advancing angle of wetting) and calculated wetting angle from*

Equations 7 and 9, θ, vs. isotropic coke content. a) is m_m-m_t before polarization (extracted from step 2) and b) is m_m-m_t after polarization (extracted from step 4).

Figure 13. *Left column: Confocal microscopy surface map before electrolysis. Right column: Contour image of the surface after electrolysis. The color red denotes "hills in the landscape" and green denotes "valleys in the landscape". Anode made of 100 % traditional anisotropic coke (0 % isotropic coke) anode, sample 1 a) and b) and sample 2 c) and d). Anode made of 49.0 % isotropic coke, sample 1 e) and f) and sample 2 g) and h). Anode made of 100 % isotropic coke, sample 1 i) and j) and sample 2 k) and l).*

Figure 14. *Ratio of true area to projected area obtained by using confocal microscopy on freshly cut and ground samples (squares) and electrolyzed samples (circles) at 1.0 A/cm^2 for 25 mins.*

Figure 15. *Raw data from EIS at 1.5 V (non-IR corrected) and LR(Q(R(LR))) modelled circuits for the corresponding raw data for anodes varying in isotropic coke content, run 1, parallel 1.*

Figure 16. *a) Calculated effective capacitance from LR(Q(R(LR))) and average double layer capacitance from the LRC circuit at high frequencies, along with one standard deviation. b) Capacitance as determined from $C_{eff,LR(Q(R(LR)))}$ and $C_{dl,high\ frequency}$ over true area/projected area after electrolysis from confocal microscopy.*